TECHNISCHE
UNIVERSITÄT
WIEN
Vienna University of Technology

DIPLOMARBEIT

A DFT+DMFT study of the electronic structure and optical properties of the blue pigment material $YIn_{1-x}Mn_xO_3$

zur Erlangung des akademischen Grades

Diplom-Ingenieur

im Rahmen des Studiums

066 461 Masterstudium Technische Physik

eingereicht von

Valentin Ransmayr, BSc

Matrikelnummer: 01526270

ausgeführt am Institut für Festkörperphysik
der Fakultät für Physik der Technischen Universität Wien

unter der Anleitung von

Dr. Anna Galler

und

Privatdoz. Dr. Jan M. Tomczak

Wien, 7. August 2022

Unterschrift Verfasser/in	Unterschrift Betreuer/in

Kurzfassung

In dieser Arbeit werden, mit Hilfe der Dichtefunktionaltheorie (DFT) und der dynamischen Molekularfeldtheorie (DMFT), die Gitterstruktur sowie die elektronischen und optischen Eigenschaften des korrelierten blauen Pigmentmaterials $YIn_{1-x}Mn_xO_3$ untersucht. Die Gitterstrukturen, in denen sich fünf O^{2-} Ionen in einer trigonalen Bipyramide (TBP) um das zentrale M^{3+} Ion koordinieren, werden in DFT und DFT+U für verschiedene Mn-Konzentrationen x relaxiert. Der Fokus liegt auf dem niedrigen x-Bereich, da dort die blaue Farbe im Experiment beobachtet wurde. Die resultierenden Strukturen werden dann zur Berechnung, im Rahmen der mBJ@DFT+DMFT Methode, der elektronischen und optischen Eigenschaften verwendet. Um Korrelationseffekte zu berücksichitgen wird die lokale Coulomb-Wechselwirkung der Mn-3d Orbitale miteinbezogen. Weiters wird das modifizierte Becke-Johnson-Potential (mBJ) in einer perturbativen Weise angewandt, um semilokale Austauschwechselwirkungen zu berücksichtigen und dadurch eine verbesserte Beschreibung der Bandlücken zu erreichen. Bei diesem Ansatz kommt die Hubbard-I Approximation zur Anwendung, um das DMFT-Impurity-Problem zu lösen.

Die Ergebnisse dieser Arbeit zeigen, dass die axialen Mn–O Bindungslängen innerhalb der TBP das Auftreten der blauen Farbe wesentlich beeinflussen, indem optische Übergänge zwischen besetzten und unbesetzten Mn-3d Zuständen selektiv ermöglicht werden. Darüber hinaus zeigen unsere Ergebnisse, dass die Zwei-Peak-Struktur in der optischen Leitfähigkeit, die für dieses blaue Material charakteristisch ist, hauptsächlich von $d-d$ Übergängen zwischen Mn-3d Zuständen stammt. Diese Zustände fallen (teilweise) in eine Bandlücke, die überwiegend zwischen den O-2p und In-5s Zuständen gebildet wird und einen Wert von ~ 4 eV für $x = 8\%$ aufweist. Die berechnete diffuse Reflektivität stimmt qualitativ gut mit dem Experiment überein, wobei es im niederenergetischen Bereich zu leichten Abweichungen kommt.

Abstract

In this work we investigate the lattice and electronic structure, as well as the optical properties of the correlated blue pigment material $YIn_{1-x}Mn_xO_3$ within density functional theory (DFT) and dynamical mean-field theory (DMFT). The lattice structures, where five O^{2-} ions coordinate in a trigonal bipyramid (TBP) around the central Mn^{3+} ion, are relaxed within DFT and DFT+U for various Mn-concentrations x. We focus on the low x regime since this is were the blue color was observed in experiments. The resulting structures are then used to calculate the electronic and optical properties within mBJ@DFT+DMFT, where an on-site Coulomb interaction of the Mn-3d states is included to incorporate correlation effects. Furthermore, the modified Becke-Johnson (mBJ) potential is applied in a perturbative way to take semilocal exchange into account for an improved description of band gaps. In this approach, we employed the Hubbard-I approximation to solve the DMFT impurity problem.

Our findings show that the axial Mn–O bond lengths within the TBP have a major impact on the occurrence of the blue color, by selectively allowing for optical transitions between occupied and unoccupied Mn-3d states. Indeed, this work shows that the two-peak structure in the optical conductivity, which is characteristic for this blue compound, arises mainly from $d-d$ transitions between Mn-3d states. These states are located within a band gap formed mainly between the O-2p and In-5s states, which has a value of ~ 4 eV for $x = 8\%$. The calculated diffuse reflectance is in qualitative good agreement with the experiment, exhibiting slight deviations in the low-energy region.

Contents

Chapter 1

Introduction

A new blue pigment material, so-called YInMn-Blue, was discovered at Oregon State University [1, 2] in 2009. The host material is $YInO_3$, where it has been observed that when a few percent of the In atoms are replaced with Mn, a brilliant blue color is formed [1]. This remarkable discovery inspired further studies, where instead of Mn other transition metals were introduced in $YInO_3$ resulting in a green [3], orange [4] and purple [5] coloration.

The properties of the blue pigment material were mostly investigated experimentally [1, 5, 6]. Despite the experimental data regarding optical properties [1, 5] as well as structural characteristics [6], it is still not clear what the mechanisms behind the color are. In particular no *ab initio* computations of the electronic structure and involved optical transitions has been presented so far. This is mainly due to the need for advanced many-body methods to capture correlation effects in the Mn-3d shell. We will fill this gap and achieve a better understanding of the mechanisms responsible for the blue coloration in $YIn_{1-x}Mn_xO_3$.

In order to calculate optical properties from first principle we need sophisticated methods to properly describe the physics within this compound. For a wide range of materials, density functional theory (DFT) [7, 8] is a well established method for *ab initio* calculations. However, DFT lacks an adequate description of correlation effects, which is extremely important for materials with electrons in open 3d-shells, such as Mn oxides. A more proper description of strongly correlated electrons can be achieved within the framework of dynamical mean-field theory (DMFT) [9, 10]. The application of DMFT to realistic materials calculations requires a combination with DFT, in the so-called DFT+DMFT [11, 12] approach. In this work, a variation of the DFT+DMFT method is employed, the so-called mBJ@DFT+DMFT [13, 14] approach, which further mimics non-local exchange.

The structure of this thesis is the following: In Chapter 2, I will present previous works and outline the current state-of-the-art. Chapter 3 focuses on the

theoretical background and introduces the methods used for the calculations of material properties. The corresponding results, including the electronic structures and optical properties, are presented in Chapter 4.

Chapter 2

A new blue pigment material: $YIn_{1-x}Mn_xO_3$

The interest in $YIn_{1-x}Mn_xO_3$ started in 2009 when A. E. Smith was studying the electronic properties of this compound and by accident discovered a bright blue color [2]. The subsequent work by A. E. Smith et al. [1] and others [6] revealed that the structure of the material is essential for the blue coloration. Stoichiometric $YMnO_3$ and $YInO_3$ usually occur as orthorhombic perovskites [15, 16]. Yet, also the synthesis of hexagonal YMO3 (M = Mn, In) is possible [17, 18]. We focus on the latter in the following.

In 1963, H. L. Yakel et al. [19] reported the occurrence of the hexagonal structure with space group $P6_3cm$ in $TMnO_3$ (T = Ho, Er, Tm, Yb, Lu, Y) and soon after ferroelectric properties were discovered in these materials [20]. Since then $YMnO_3$ has been investigated extensively, mostly due to its ferroelectric transition at $T_{FE} \approx 923$ K [21] and its antiferromagnetic ordering below $T_N = 75$ K [22].

Fig. 2.1 illustrates the hexagonal structure, where layers of Y^{3+} ions (green) alternate layers of MO_5 (M = Mn, In) polyhedra. Here, the O^{2-} anions (red) coordinate in trigonal bipyramids (TBP) around the central M^{3+} cations (purple). In this TBP-coordination (right side of Fig. 2.1) the central M^{3+} ion forms three equatorial bonds with O^{2-} and two out-of-plane axial bonds. These axial and equatorial bonds will be referred to as M–O_{ax} and M–O_{eq}, respectively. Note that for hexagonal $YMnO_3$ a tilting of the Mn–O_{ax} bonds and a buckling of the TBP, along with a shift of the Y^{3+} ions, is observed, where the latter leads to a ferroelectric polarization [23].

After the accidental discovery in 2009, the work by A. E. Smith et al. [1] showed that $YIn_{1-x}Mn_xO_3$ exhibits a blue coloration for low Mn concentrations x. Fig. 2.2(a) displays the colors of the powders and Fig. 2.2(b) shows the associated diffuse reflectance spectra for various different x, measured in Ref. [1].

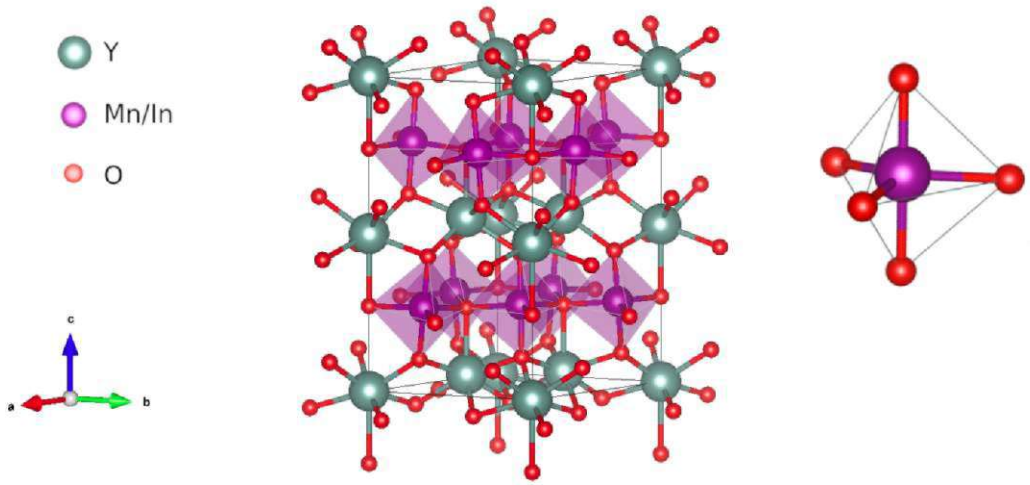

Fig. 2.1: The structure of hexagonal YMO_3, where M = Mn or In. Own illustration, where VESTA [24] was used to plot the structure file of Ref.[25], which is based on experimental data of Ref.[26].

We can see from Fig. 2.2(b) that pure $YInO_3$ ($x = 0$) exhibits no absorption up to $\sim$ 3.8 eV, while $YMnO_3$ ($x = 1$) absorbs over the entire visible range of the light spectrum, which leaves these materials white and black, respectively. For low Mn-concentrations, e.g., $x = 5\%$, one observes two absorption peaks. One centered around $\sim$ 2 eV, absorbing from the red to the green region, and a second absorption feature with its peak around $\sim$ 3.5 eV [1]. Only blue is reflected, in the limit of small x, explaining the color of the compound. Fig. 2.2(b) shows that increasing the Mn-concentration results in a broadening of the first absorption peak and a shift of the second one to lower energies, yielding a darker color [1].

The authors of Ref. [1] speculated that the first absorption peak arises due to a transition from occupied O-$2p_{x,y}$ and Mn-$3d_{x^2-y^2}/d_{xy}$ states to the lowest unoccupied Mn-$3d_{z^2}$ states, which are positioned in the band gap of $YInO_3$. The second absorption peak was interpreted as a transition from occupied O-$2p$ to the unoccupied Mn-$3d_{z^2}$ states [1].

Although these results and considerations might seem reasonable, the theoretical study does not report any theoretical spectra nor calculations of the optical properties. Additionally, the LSDA+U calculations of Ref. [1] assume an antiferromagnetic ordering, while experiments show that $YIn_{1-x}Mn_xO_3$ is paramagnetic at room temperature [27]. Furthermore, it is known that the LSDA+U approach can not correctly describe the multiplet splitting [28] of the Mn-$3d$ states. In Ref. [1] the structure was relaxed in LSDA+U for $x = 0, 0.25, 0.5, 0.75, 1$. The reported

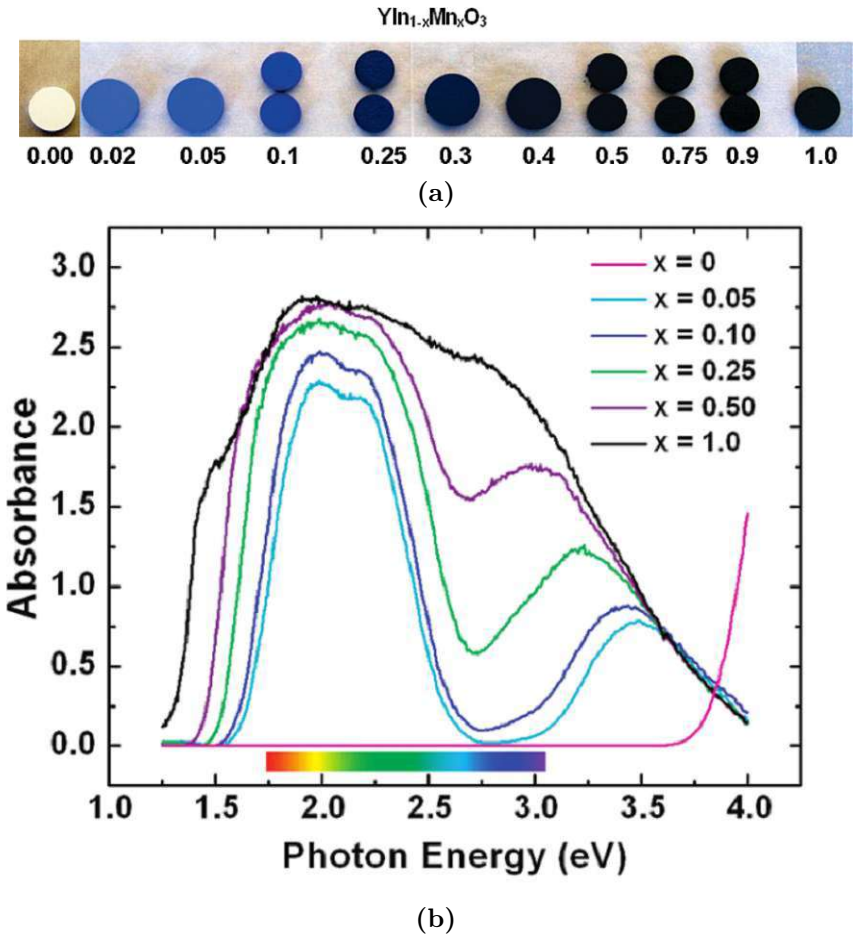

Fig. 2.2: (a) Pellets of $YIn_{1-x}Mn_xO_3$ at different Mn-concentrations x. Figure adapted from Figure 3 of Ref. [1]. (b) Diffuse reflectance spectra for various x. Illustration taken from Figure 4 of Ref. [1].

M–O_{eq} distances for $x = 0.25$ and 0.75 are similar, while the In–O_{ax} and Mn–O_{ax} bond lengths differ with values comparable to those of pure $YInO_3$ and $YMnO_3$, respectively [1].

As suggested by Ref. [1], the Mn–O bond lengths in the TBP-coordination plays an important role for the properties of $YIn_{1-x}Mn_xO_3$, since they influence the crystal-field splitting of the Mn-3d orbitals. S. Mukherjee et al. [6] investigated the local environment of M^{3+} ions in this compound experimentally, reporting unit cell parameters, as well as axial and equatorial M–O bond lengths for various Mn-concentrations. The measurements show that for the pure end members the main difference in the MO_5 polyhedra are the M–O_{ax} bonds, which are $\sim$ 1.86 Å for Mn–O_{ax} and $\sim$ 2.09 Å for In–O_{ax} bonds [6]. This makes sense since Mn^{3+} is smaller

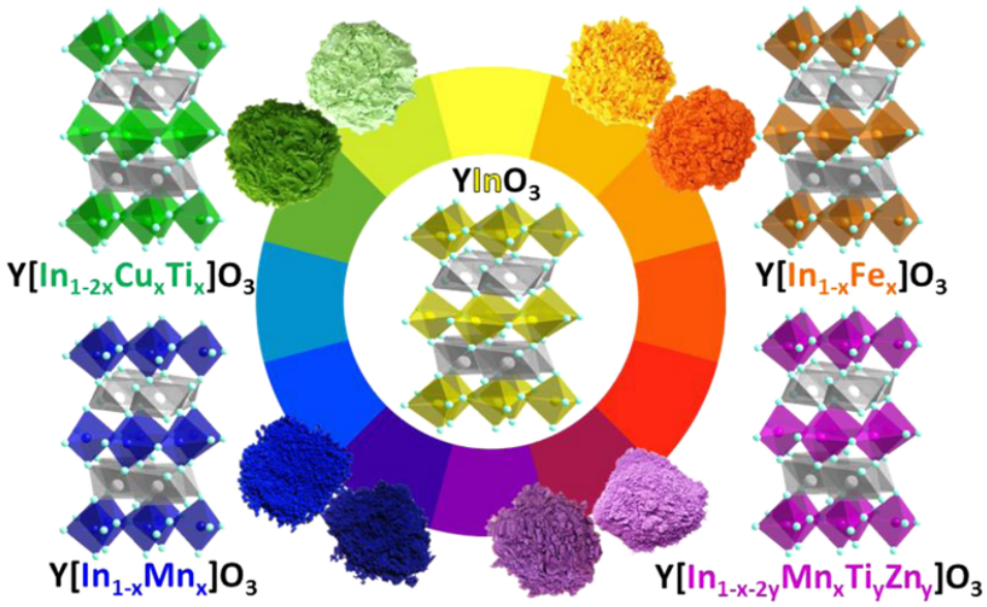

Fig. 2.3: Color cycle of hexagonal $YInO_3$ substituted with different transition metals. Figure taken from Figure 2 of Ref. [5].

than the In^{3+} ion. Increasing x in $YIn_{1-x}Mn_xO_3$ results in an overall decrease of the bond lengths, while it is observed that the M–O_{eq} decrease less than the M–O_{ax} bond lengths [6]. Furthermore, the bond lengths differ more in the MnO_5 polyhedra than in the InO_5 TBP, when comparing the low Mn-concentrations to Mn-rich environments [6].

For low x, where the blue color is observed, the TBP are strongly distorted along the axial direction [6]. As a consequence two different Mn–O_{ax} bond lengths are observed, which are ~ 1.88 Å and ~ 2.09 Å [6] in the case of $x = 5\%$. This distortion, resulting in asymmetric axial bond lengths, has been considered in Ref. [6] to be important for the appearance of the blue color in the low Mn-concentration limit.

Ref. [6] reported two rather similar (symmetric) Mn–O_{ax} bond lengths for pure $YMnO_3$ and proposed that for arbitrary x the local Mn^{3+}-environments are made of two different MnO_5 polyhedra. One with asymmetric axial bond lengths, dominating in the low Mn-concentration regime and the other one with symmetric Mn–O_{ax} distances for higher concentrations [6]. In this picture the shift of the second absorption peak in Fig. 2.2(b) to lower energies with growing Mn-concentration can be ascribed to the increasing occurrence of the TBP with symmetric bond lengths [6].

The discovery of the blue color in $YIn_{1-x}Mn_xO_3$ [1] triggered a series of further experiments, substituting other transition metals onto the TBP sites of $YInO_3$, in

order to generate different colors. As a result, these experiments revealed colors ranging from green in $YIn_{1-2x}Cu_xTi_xO_3$ [3], over orange in $YIn_{1-x}Fe_xO_3$ [4] to purple in $YIn_{1-x-2y}Mn_xTi_yZn_yO_3$ [5]. Fig. 2.3 (taken from Ref. [5]) shows the range of colors covered. For the purple pigment it is believed that the change in color is a result of decreased Mn–O_{ax} bond lengths, which impacts the crystal field splitting and therefore the energy of the $d-d$ transition responsible for the color [5].

To understand the mechanisms behind the blue color in $YIn_{1-x}Mn_xO_3$, we perform detailed calculations using the mBJ@DFT+DMFT [13, 14] approach, in order to investigate the involved optical transitions. With this method we can address the paramagnetic phase of the compound and tackle the strongly correlated Mn$-d$ states, as well as ligand $p-$bands within an *ab initio* framework. In addition, crystal-field effects and the multiplet splitting of the $d-$states are incorporated within this approach making a decisive step towards a proper modeling of this fascinating compound.

Chapter 3

Methods

In order to calculate a material's electronic structure, we start from the well-known solid state Hamiltonian in the Born-Oppenheimer [29] approximation, which separates lattice and electronic degrees of freedom,

$$H = \sum_i \left[-\frac{\hbar^2 \triangle_i}{2m_e} - \sum_j \frac{e^2}{4\pi\epsilon_0} \frac{Z_j}{|\mathbf{r}_i - \mathbf{R}_j|} \right] + \frac{1}{2} \sum_{i \neq i'} \frac{e^2}{4\pi\epsilon_0} \frac{1}{|\mathbf{r}_i - \mathbf{r}_{i'}|} , \tag{3.1}$$

where $\mathbf{r}_i$ ($\mathbf{R}_j$) is the position of the electron i (ion j) with charge e ($Z_j e$). Here, ϵ_0, $\hbar$ and e are the dielectric constant, the reduced Planck constant and the elementary charge, respectively. The first term is the kinetic energy of the electrons, where $\triangle_i$ denotes the Laplace operator and m_e is the mass of the electrons. The second term describes the attractive lattice potential between electrons and ions and the last term accounts for the repulsive Coulomb interaction between electrons. In the following we use atomic units with $\hbar = e = m_e = (4\pi\epsilon_0)^{-1} = 1$, unless noted otherwise.

The Born-Oppenheimer [29] approximation assumes that, due to the fact that electrons and ions move on different time scales (since the ionic mass is much larger), we can separate the electronic and ionic degrees of freedom. The ions of the crystal lattice then form a static potential for the electrons [29]. Another assumption we make is to neglect relativistic corrections, which is justified since in $YIn_{1-x}Mn_xO_3$ the elements are not too heavy such that spin-orbit coupling plays no role (in particular for the low-energy states).

Still, the solid state Hamiltonian in Eq. (3.1) can not be solved without further simplifications. This is due to the third term in Eq. (3.1), which generates correlations between electrons and makes the problem scale exponentially with the number of electrons, therefore making it impossible to solve it analytically or numerically for realistic materials with a large number of electrons. In order to overcome this problem one needs to make further approximations, which we introduce in the following.

3.1 Density functional theory (DFT)

Density functional theory (DFT) is based on the ground state electron density $\rho(\mathbf{r})$. DFT started with P. Hohenberg and W. Kohn, who showed in Ref. [7] that for an interacting electron gas in an external potential $v(\mathbf{r})$ the ground state energy E is a unique functional of $\rho(\mathbf{r})$, with its minimum at the ground-state electron density $\rho_0(\mathbf{r})$. Furthermore, they showed that $E[\rho]$ can be written as [7]:

$$E[\rho] = \int v(\mathbf{r})\rho(\mathbf{r})\, d^3r + \frac{1}{2}\int\int \frac{\rho(\mathbf{r})\rho(\mathbf{r}')}{|\mathbf{r}-\mathbf{r}'|}\, d^3r\, d^3r' + G[\rho]\,, \tag{3.2}$$

where $G[\rho]$ is a functional of ρ, which should include the effects of electron-electron interactions as well as the kinetic energy. The first term is the energy due to the external lattice potential and the second term is the classical Coulomb energy.

3.1.1 Kohn-Sham equations

In Ref. [8], W. Kohn and L. J. Sham mapped the interacting problem onto a system of non-interacting electrons with the same density, resulting in a set of self-consistent equations for the ground state energy and electron density. $G[\rho]$ is expressed as the sum of the kinetic energy of non-interacting electrons $T[\rho]$ and the (unkown) exchange and correlation energy of interacting electrons $E_{xc}[\rho]$ [8]. In order to find the ground state electron density $\rho_0(\mathbf{r})$, $E[\rho]$ is minimized leading to effective one-electron equations, the so-called Kohn-Sham equations [8]:

$$\begin{aligned}\left[-\frac{\triangle}{2} + v_{eff}(\mathbf{r})\right]\psi_i(\mathbf{r}) &= \varepsilon_i\psi_i(\mathbf{r})\ \text{, with}\\ v_{eff}(\mathbf{r}) &= v(\mathbf{r}) + \int \frac{\rho(\mathbf{r}')}{|\mathbf{r}-\mathbf{r}'|}\, d^3r' + \frac{\delta E_{xc}[\rho]}{\delta\rho}\ \text{and}\\ \rho(\mathbf{r}) &= \sum_{i=1}^{N} |\psi_i(\mathbf{r})|^2\ ,\end{aligned} \tag{3.3}$$

where N is the number of electrons and $\psi_i(\mathbf{r})$ are the so-called Kohn-Sham orbitals with associated eigenenergies ε_i. Here, the effective potential $v_{eff}(\mathbf{r})$ contains the lattice potential $v(\mathbf{r})$, a Hartree term, describing a mean-field generated by all electrons and the last term which is the potential arising due to electronic exchange and correlation. Note that the exchange and correlation energy $E_{xc}[\rho]$ is not known exactly and therefore reasonable approximations are crucial. These N one-particle Schrödinger equations with an effective potential $v_{eff}(\mathbf{r})$ have to be solved self-consistently. In principle, the resulting $\rho(\mathbf{r})$ and $E[\rho]$ are only valid for the ground state and the $\psi_i(\mathbf{r})$ and ε_i do not have any physical meaning.

However, the eigenvalues of the Kohn-Sham-Hamiltonian ε_i are often interpreted as one-particle eigenenergies that give rise to an electronic band structure.

3.1.2 Local Density approximation (LDA)

Approximations to $E_{xc}[\rho]$ need to be made in order to solve the Kohn-Sham equations (Eq. (3.3)). In the local density approximation (LDA), $E_{xc}[\rho]$ is defined as [8],

$$E_{xc}[\rho] = \int \epsilon_{xc}^{LDA}(\rho(\mathbf{r}))\rho(\mathbf{r})d^3r \ . \tag{3.4}$$

Here, $\epsilon_{xc}^{LDA}(\rho(\mathbf{r}))$ is the exchange and correlation energy per particle of a uniform electron gas. $\epsilon_{xc}^{LDA}(\rho(\mathbf{r}))$ and consequently $E_{xc}[\rho]$ depend only on the local electron density $\rho(\mathbf{r})$. An attempt to include non-local effects through the derivative of $\rho(\mathbf{r})$ is the generalized gradient approximation (GGA)[30, 31, 32]. It should be noted that for spin-polarized calculations the energy functional in Eq. (3.4) and therefore also the Kohn-Sham equations (Eq. (3.3)) depend on the spin-up and spin-down electron density, denoted by $\rho_\uparrow(\mathbf{r})$ and $\rho_\downarrow(\mathbf{r})$ respectively, with $\rho(\mathbf{r}) = \rho_\uparrow(\mathbf{r}) + \rho_\downarrow(\mathbf{r})$. Such a case is referred to as local spin density approximation (LSDA).

3.1.3 LSDA+U

A possibility to improve the LDA description for strong on-site correlation effects in partially filled d and f shells was introduced by V. I. Anisimov et al. [33] in the so-called LSDA+U method. For which the total energy functional within LDA is corrected by an orbital dependent interaction for correlated states (e.g. $4f$ or $3d$ orbitals) [33].

In a subsequent publication by V. I. Anisimov et al.[34] the LSDA+U approach was further improved. In this formulation the energy functional consists of three parts [34]:

$$E = E^{LDA} - E^{DC} + E^{U} \ . \tag{3.5}$$

The LDA energy functional E^{LDA} as discussed in Sec. 3.1.2. The second part is a so-called double counting energy E^{DC}, which is subtracted from E^{LDA} to account for the interaction which are already included in LDA. The last part is the on-site Coulomb interaction, which, here, takes the form of a density-density interaction [34]

$$E^{U} = \frac{1}{2}\sum_{lm\sigma} U_{lm} n_{l\sigma} n_{m\bar{\sigma}} + \frac{1}{2}\sum_{\substack{lm\sigma \\ l\neq m}} (U_{lm} - J_{lm}) n_{l\sigma} n_{m\sigma} \ . \tag{3.6}$$

Here, $n_{l\sigma}$ is the occupancy of orbital l with spin σ ($\bar{\sigma}$ denotes the opposite spin of σ). U_{lm} and J_{lm} are the Coulomb and exchange interaction matrices.

Different versions of the LSDA+U approach are implemented in the *WIEN2k* package [35, 36] and we will use the formulation from Ref. [34], which is the fully localized limit version (within the *WIEN2k* package it is also referred to as the "LDA+U(SIC)", where SIC means self-interaction correction).

3.1.4 modified Becke-Johnson (mBJ) potential

In order to effectively incorporate non-local exchange F. Tran and P. Blaha proposed in Ref. [37] a modified version of the Becke-Johnson [38] potential for exchange, which will be referred to as TB-mBJ in the following. The potential represents an improvement for certain materials, in particular semiconductors, where LDA usually underestimates the band gap. It is given in Ref. [37] via

$$\begin{aligned} v_x^{mBJ}(\mathbf{r}) &= c v_x^{BR}(\mathbf{r}) + (3c-2)\frac{1}{\pi}\sqrt{\frac{10t(\mathbf{r})}{12\rho(\mathbf{r})}} \text{ , with} \\ c &= \alpha + \beta\sqrt{\frac{1}{V_{cell}}\int_{cell}\frac{|\nabla\rho(\mathbf{r}')|}{\rho(\mathbf{r}')}d^3r'}. \end{aligned} \tag{3.7}$$

Here, $t(\mathbf{r}) = \frac{1}{2}\sum_i^N \nabla\psi_i^* \cdot \nabla\psi_i$ is the kinetic-energy density and $v_x^{BR}(\mathbf{r})$ is the Becke-Roussel [39] potential. α and β are empirical parameters, which were determined in Ref. [37] by fitting the band gap for a set of solids, and the second term includes the average of $\frac{|\nabla\rho(\mathbf{r}')|}{\rho(\mathbf{r}')}$ in the unit cell with volume V_{cell}.

We note that the investigation of several different exchange and correlation functionals in benchmark studies [40, 41] have shown, that the TB-mBJ potential is well suited for the determination of band gaps in semiconductors.

3.1.5 Basis sets

The Kohn-Sham orbitals ψ_i in Eq. (3.3), with $i = (n, \mathbf{k})$ where $\mathbf{k}$ is the momentum and n denotes the band index, can be expanded in an arbitrary basis ϕ_i as

$$\psi_{n\mathbf{k}}(\mathbf{r}) = \sum_i c_{n\mathbf{k}}^i \phi_i(\mathbf{r}) \ . \tag{3.8}$$

The choice of the basis in particular affects the computational effort and must be taken with care. J. C. Slater introduced in Ref. [42] the augmented plane wave (APW) method, where the unit cell is divided into two regions. One region is defined by spheres surrounding each atom in the unit cell with a characteristic muffin-tin radius R_{MT}. Inside these spheres atomic orbitals are used, while outside (interstitial region) plane waves are utilized. Additionally, the description in both regions must match at the sphere boundaries. Since the APW method is

computationally costly, a linearization was introduced by O. K. Andersen in Ref. [43], which leads to the linearized-APW [44] (LAPW) method. Subsequently to the LAPW method, other approaches were developed, among them the APW+lo method by E. Sjöstedt et al.[45], which is also implemented in the *WIEN2k* [35, 36] program.

Wannier functions

Since the next section will focus on a many body approach, we want to introduce a different set of basis functions, with a higher degree of localization. Orbitals with this property are the Wannier functions $|w_{n\mathbf{R}}\rangle$, which are defined via the Fourier transform of the Bloch states $|\psi_{n\mathbf{k}}\rangle$ [46]:

$$|w_{n\mathbf{R}}\rangle = \frac{1}{\sqrt{N_{\mathbf{k}}}} \sum_{\mathbf{k}} e^{-i\mathbf{k}\mathbf{R}} |\psi_{n\mathbf{k}}\rangle \ , \tag{3.9}$$

where $\mathbf{R}$ is the lattice translation vector and $N_{\mathbf{k}}$ is the number of $\mathbf{k}$-points in the Brillouin zone (BZ). In general, these Wannier functions are not uniquely defined via Eq. (3.9) and therefore different methods can be used to construct them, where we will focus on the projective Wannier function method [47]. Here we consider a basis set of non-orthogonal Wannier functions in $\mathbf{k}$-space $|\tilde{w}_{n\mathbf{k}}\rangle$ as [47]

$$|\tilde{w}_{n\mathbf{k}}\rangle = \sum_{i=n_{bot}}^{n_{top}} \langle \psi_{i\mathbf{k}} | \chi_n \rangle \, |\psi_{i\mathbf{k}}\rangle \, , \tag{3.10}$$

with the Kohn-Sham orbitals $|\psi_{i\mathbf{k}}\rangle$ within an energy window $\mathcal{W} = [\epsilon_{bot}, \epsilon_{top}]$. Here, n_{bot} and n_{top} are the band indices corresponding to ϵ_{bot} and ϵ_{top}, respectively and $|\chi_n\rangle$ are atomic-like orbitals, which are centered around the atom sites. The orthogonal Wannier functions $|w_{n\mathbf{k}}\rangle$ can be calculated as [47]

$$|w_{n\mathbf{k}}\rangle = \sum_{n'} O^{-\frac{1}{2}}_{nn'}(\mathbf{k}) \, |\tilde{w}_{n'\mathbf{k}}\rangle \, , \tag{3.11}$$

where $O_{nn'}(\mathbf{k}) = \langle \tilde{w}_{n\mathbf{k}} | \tilde{w}_{n'\mathbf{k}} \rangle$ is the overlap matrix.

For the description of many body correlations, we will use the *TRIQS* [48] program package, in particular *TRIQS/DFTTools* [49], which provides an interface with *WIEN2k*. The interface is the program *dmftproj*, where the projective Wannier functions are calculated from the *WIEN2k* Kohn-Sham orbitals, as described in Ref. [50].

3.2 Correlation effects: a many-body approach

The DFT approach of Sec. 3.1 works within an effective single particle picture and therefore can not capture the full complexity of the many-body Hamiltonian in Eq. (3.1). In the following, we focus on many-body methods to incorporate correlation effects, in particular the dynamical mean-field theory (DMFT).

3.2.1 Hubbard model

A model to study the interaction between electrons was developed by M.C. Gutzwiller [51], J. Hubbard [52] and J. Kanamori [53]. The Hamiltonian of this so-called single-band Hubbard model is given by [52]

$$\hat{H} = \sum_{ij\sigma} t_{ij} \hat{c}^{\dagger}_{i\sigma} \hat{c}_{j\sigma} + U \sum_{i} \hat{n}_{i\uparrow} \hat{n}_{i\downarrow}, \tag{3.12}$$

with $\hat{n}_{i\sigma} = \hat{c}^{\dagger}_{i\sigma} \hat{c}_{i\sigma}$, where $\hat{c}^{\dagger}_{i\sigma}$ ($\hat{c}_{i\sigma}$) are creation (annihilation) operators, which create (annihilate) an electron with spin σ at lattice site i. The hopping amplitude t_{ij} gives the probability of electrons to hop from lattice site i to j, while U represents the Coulomb repulsion between electrons with opposite spin at lattice site i.

In order to generalize the Hamiltonian in Eq. (3.12) to multi-orbital systems, we follow the approach by A. M. Oleś in Ref. [54], where a multi-orbital Hubbard model was derived to treat correlations in transition-metal d-orbitals. We write the solid state Hamiltonian in Eq. (3.1) in second quantization, using the field operators $\hat{\Psi}_{\sigma}(\mathbf{r})$ and $\hat{\Psi}^{\dagger}_{\sigma}(\mathbf{r})$ [1] as

$$\begin{aligned} \hat{H} = & \sum_{\sigma} \int d^3r \hat{\Psi}^{\dagger}_{\sigma}(\mathbf{r}) \left[-\frac{\triangle}{2} - \sum_{j} \frac{Z_j}{|\mathbf{r} - \mathbf{R}_j|} \right] \hat{\Psi}_{\sigma}(\mathbf{r}) \\ & + \frac{1}{2} \sum_{\sigma\sigma'} \int \int d^3r d^3r' \hat{\Psi}^{\dagger}_{\sigma}(\mathbf{r}) \hat{\Psi}^{\dagger}_{\sigma'}(\mathbf{r}') \frac{1}{|\mathbf{r} - \mathbf{r}'|} \hat{\Psi}_{\sigma'}(\mathbf{r}') \hat{\Psi}_{\sigma}(\mathbf{r}) \ , \end{aligned} \tag{3.13}$$

where $\hat{\Psi}_{\sigma}(\mathbf{r})$ ($\hat{\Psi}^{\dagger}_{\sigma}(\mathbf{r})$) are linear combinations of the creation and annihilation operators:

$$\hat{\Psi}^{(\dagger)}_{\sigma}(\mathbf{r}) = \sum_{\alpha} \phi^{(*)}_{\alpha}(\mathbf{r}) \, \hat{c}^{(\dagger)}_{\sigma\alpha} \ . \tag{3.14}$$

Here, $\hat{c}^{\dagger}_{\sigma\alpha}$ ($\hat{c}_{\sigma\alpha}$) creates (annihilates) an electron with spin σ and wave function ϕ_{α} (ϕ^{*}_{α}). In the following, we choose the Wannier-functions w_{im} for our basis, such

[1] For an introduction to the formalism of second quantization and field operators, see, e.g., Ref. [55], Chap. 1 and 2.

that $\phi_\alpha = w_{im}$ and $\hat{c}^{(\dagger)}_{\sigma\alpha} = \hat{c}^{(\dagger)}_{\sigma im}$, where i denotes the site index and m is the orbital index. Inserting Eq. (3.14) in Eq. (3.13) and neglecting non-local contributions to the Coulomb repulsion (since on-site interactions are dominant as pointed out by J. Hubbard in Ref. [52]) yields

$$\hat{H} = \sum_{\sigma} \sum_{\boldsymbol{ilj}m} t_{\boldsymbol{ilj}m}\, \hat{c}^{\dagger}_{\sigma \boldsymbol{i}l}\, \hat{c}_{\sigma \boldsymbol{j}m} + \frac{1}{2} \sum_{\sigma\sigma'} \sum_{\boldsymbol{i}ll'mm'} U_{ll'mm'}\, \hat{c}^{\dagger}_{\sigma \boldsymbol{i}l}\, \hat{c}^{\dagger}_{\sigma' \boldsymbol{i}l'} \hat{c}_{\sigma' \boldsymbol{i}m}\, \hat{c}_{\sigma \boldsymbol{i}m'} \ , \tag{3.15}$$

with the hopping amplitude $t_{\boldsymbol{ilj}m}$ defined as

$$t_{\boldsymbol{ilj}m} = \int w^*_{\boldsymbol{i}l}(\mathbf{r}) \left[-\frac{\triangle}{2} - \sum_{\boldsymbol{i}'} \frac{Z_{\boldsymbol{i}'}}{|\mathbf{r} - \mathbf{R}_{\boldsymbol{i}'}|} \right] w_{\boldsymbol{j}m}(\mathbf{r})\, d^3r \tag{3.16}$$

and the general local Coulomb interaction $U_{mm'll'}$ given via

$$U_{ll'mm'} = \int\int w^*_{\boldsymbol{i}l}(\mathbf{r}) w^*_{\boldsymbol{i}l'}(\mathbf{r}') \frac{1}{|\mathbf{r} - \mathbf{r}'|} w_{\boldsymbol{i}m}(\mathbf{r}') w_{\boldsymbol{i}m'}(\mathbf{r})\, d^3r d^3r' \ . \tag{3.17}$$

The first term of Eq. (3.15) is the one-electron hopping of the solid state Hamiltonian and will be denoted by $\hat{H}^0$ in the following. We can write $\hat{H}^0$ in terms of creation and annihilation operators in $\mathbf{k}$-space, where the connection is given via a Fourier transformation, such that $\hat{c}_{\sigma im} = \frac{1}{\sqrt{N_L}} \sum_i \hat{c}_{\sigma \mathbf{k}m} e^{-i\mathbf{k}\mathbf{R}_i}$ (N_L is the number of lattice sites). Inserting this in $\hat{H}^0$ yields

$$\begin{aligned} \hat{H}^0 &= \sum_{\sigma\mathbf{k}} \varepsilon_{\mathbf{k}lm}\, \hat{c}^{\dagger}_{\sigma\mathbf{k}l}\, \hat{c}_{\sigma\mathbf{k}m} \ , \text{ with} \\ \varepsilon_{\mathbf{k}lm} &= \frac{1}{N_L} \sum_{ij} t_{\boldsymbol{ilj}m}\, e^{i\mathbf{k}(\mathbf{R}_i - \mathbf{R}_j)} \ . \end{aligned} \tag{3.18}$$

Here, $\varepsilon_{\mathbf{k}lm}$ are the one-electron transfer energies, which are in general a matrix in the orbital indices l and m.

3.2.2 Dynamical mean field theory (DMFT)

In this section, we introduce the dynamical mean-field theory (DMFT), a Green's function based many-body method. For the sake of completeness, we will shortly define the Green's function [2] here. In the following, we either use Green's functions as a function of real time t or imaginary time τ and their associated Fourier transformed Green's functions depending on frequencies ω or Matsubara frequencies ω_ν (with $\omega_\nu = (2\nu + 1)\pi/\beta$ and $\beta = (k_B T)^{-1}$), respectively. The analytical

[2] For a more detailed introduction to Green's function, see e.g., Ref. [55].

continuation connects the representation in real-time/frequencies with the one in imaginary-time/Matsubara frequencies. The real-time Green's function is defined as

$$G_{iljm}(t-t') = -i\left\langle T\hat{c}_{il\sigma}(t)\hat{c}^{\dagger}_{jm\sigma}(t')\right\rangle \ , \tag{3.19}$$

while the imaginary-time Green's function is

$$G_{iljm}(\tau-\tau') = -\left\langle T\hat{c}_{il\sigma}(\tau)\hat{c}^{\dagger}_{jm\sigma}(\tau')\right\rangle \ . \tag{3.20}$$

Here, $\hat{c}_{i\sigma}(t) = e^{i\hat{H}t}\hat{c}_{i\sigma}e^{-i\hat{H}t}$ ($\hat{c}_{i\sigma}(\tau) = e^{\hat{H}\tau}\hat{c}_{i\sigma}e^{-\hat{H}\tau}$) and T is the time-ordering operator with respect to t (τ). Bold symbols denote matrices in the orbital indices l and m, e.g. $\boldsymbol{G}_{ij} = G_{iljm}$. The expectation value $\langle ...\rangle$ of an operator $\hat{O}$ is defined as

$$\left\langle \hat{O}\right\rangle = \frac{\mathrm{Tr}\left(e^{-\beta\hat{H}}\hat{O}\right)}{\mathrm{Tr}\left(e^{-\beta\hat{H}}\right)}, \tag{3.21}$$

with the inverse temperature $\beta = (k_B T)^{-1}$.

We introduce the DMFT following the derivation in Ref. [56]. The starting point is the Hubbard Hamiltonian in Eq. (3.15), for which DMFT is used to solve it in the limit of infinite dimensions.

Scaling of the Hubbard model for $d \to \infty$

The Hubbard model in infinite dimension d was first investigated by W. Metzner and D. Vollhardt in Ref. [10]. We note that increasing dimensions can also be understood as increasing the number of equivalent neighboring lattice sites. Since the interacting part of the Hubbard model is purely local, the associated energy per site stays finite in infinite dimensions:

$$\left\langle \sum_{\substack{\sigma\sigma'\\ ll'mm'}} U_{ll'mm'}\,\hat{c}^{\dagger}_{\sigma il}\,\hat{c}^{\dagger}_{\sigma' il'}\hat{c}_{\sigma' im}\,\hat{c}_{\sigma im'}\right\rangle = const.\ \text{for}\ d\to\infty\ . \tag{3.22}$$

The scaling of the kinetic energy (first term in Eq. (3.15)), is not instead, trivial, since it includes the summation over neighboring sites. This sum scales linearly with d and would diverge for $d \to \infty$. As shown in Ref. [10], only the scaling

$$t_{iljm} = \frac{t^*_{iljm}}{\sqrt{2d}} \ \text{with}\ t^*_{iljm} = const.\ \text{for}\ d\to\infty \tag{3.23}$$

results in a non-trivial model with competing kinetic and Coulomb energy. Hence it follows that $\left\langle \hat{c}^{\dagger}_{il\sigma}\hat{c}_{jm\sigma}\right\rangle$ must scale like

$$\left\langle \hat{c}^{\dagger}_{il\sigma}\hat{c}_{jm\sigma}\right\rangle \propto \frac{1}{\sqrt{d}} \ \text{for}\ d\to\infty \tag{3.24}$$

so that the kinetic energy does not diverge. This scaling determines the diagrammatic content of the DMFT self-energy Σ.

Local self-energy $\boldsymbol{\Sigma}$

Dyson's equation defines the self-energy $\boldsymbol{\Sigma}$ and connects the interacting Green's function $\boldsymbol{G}$ with the non-interacting one $\boldsymbol{G}^0$ via

$$\boldsymbol{G}_{ij}(\tau) = \boldsymbol{G}^0_{ij}(\tau) + \sum_{i'j'} \int_0^\beta \int_0^\beta \boldsymbol{G}^0_{ii'}(\tau')\boldsymbol{\Sigma}_{i'j'}(\tau'' - \tau')\boldsymbol{G}_{j'j}(\tau - \tau'')d\tau' d\tau'', \tag{3.25}$$

which reads, after a Fourier transformation and rearrangement,

$$\boldsymbol{G}_{\mathbf{k}}(i\omega_\nu)^{-1} = \boldsymbol{G}^0_{\mathbf{k}}(i\omega_\nu)^{-1} - \boldsymbol{\Sigma}_{\mathbf{k}}(i\omega_\nu). \tag{3.26}$$

The Dyson equation can be graphically expressed as

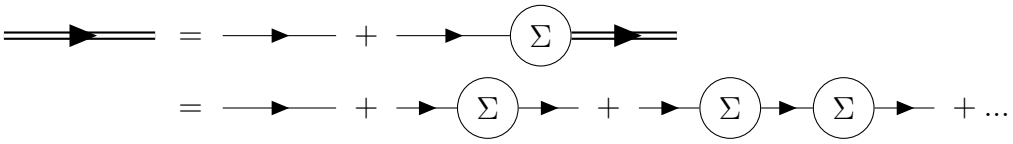

where the double lines correspond to the interacting and the single line to the non-interacting Green's function.

A consequence of the above analysis is that the non-interacting Green's function $\boldsymbol{G}^0$ scales with a factor of $d^{-1/2}$ for $d \to \infty$ [10]. Consequently, contributions from non-local diagrams are suppressed and the self-energy is purely local [10]. In order to depict this we consider an example in Fig. 3.1(a), which shows a second-order Feynman diagram for the Green function. For $i \neq j$, the sites are connected by three non-interacting Green function $\boldsymbol{G}^0$ lines. This contribution scales with a factor $d^{-3/2}$ and can thus be neglected in the limit of infinite dimensions.

Nevertheless, different lattice sites can also be connected via two single lines as depicted on the left side of Fig. 3.1(b). The d^{-1} factor from the two single lines and the d^1 from the sum over neighboring sites would result in an overall constant scaling for $d \to \infty$. But this diagram is not irreducible and can be rewritten in terms of the interacting Green function $\boldsymbol{G}_{ij}$ as depicted on the right side of Fig. 3.1(b). Therefore, this contribution is already contained in the local interacting Green function $\boldsymbol{G}_{ii}$.

Consequently, the self-energy is purely local

$$\boldsymbol{\Sigma}_{ij}(\omega) = \boldsymbol{\Sigma}(\omega)\delta_{ij} \text{ for } d \to \infty\ , \tag{3.27}$$

or, in other words, $\mathbf{k}$-independent $\boldsymbol{\Sigma}_{\mathbf{k}}(\omega) = \boldsymbol{\Sigma}(\omega)$.

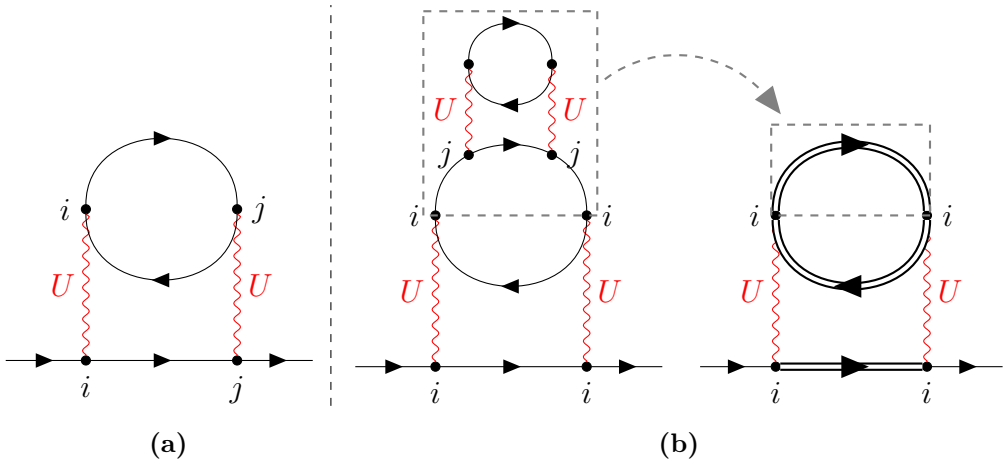

Fig. 3.1: Feynman diagrams for the Green function. **(a)** The lattice sites i and j are connected by three Green functions (single lines). **(b)** On the left side, i and j are connected by only two single lines. But this diagram is included in the one on the right side, where the interacting Green function is denoted by double lines. The latter is a purely local diagram. Own illustration, adapted from Fig. 5 and Fig. 6 of Ref. [56].

The Anderson impurity model

Georges and Kotliar showed in Ref. [9] that the Hubbard model in the limit of infinite dimensions can be mapped onto an Anderson impurity model [57](AIM). The Hamiltonian of the AIM [57] for multiple orbitals can be written as

$$\begin{aligned}\hat{H}^{AIM} = &\sum_{\mathbf{k}\sigma l} \epsilon_{\mathbf{k}l} \hat{a}^{\dagger}_{\mathbf{k}\sigma l} \hat{a}_{\mathbf{k}\sigma l} + \sum_{\sigma m} \epsilon_m \hat{c}^{\dagger}_{\sigma m} \hat{c}_{\sigma m} + \sum_{\mathbf{k},\sigma lm} [V_{\mathbf{k}lm} \hat{a}^{\dagger}_{\mathbf{k}\sigma l} \hat{c}_{\sigma m} + h.c.] \\ &+ \frac{1}{2} \sum_{ll'mm'}^{\sigma\sigma'} U_{ll'mm'}\, \hat{c}^{\dagger}_{\sigma l}\, \hat{c}^{\dagger}_{\sigma' l'} \hat{c}_{\sigma' m}\, \hat{c}_{\sigma m'} \ .\end{aligned} \tag{3.28}$$

Here, $\hat{c}^{\dagger}_{\sigma}$ ($\hat{c}_{\sigma}$) creates (annihilates) an electron at the impurity site with spin σ. In the context of DMFT, the $\hat{a}^{\dagger}_{\mathbf{k}\sigma l}$ ($\hat{a}_{\mathbf{k}\sigma l}$) describe a particle reservoir (bath), where $\hat{a}^{\dagger}_{\mathbf{k}\sigma l}$ ($\hat{a}_{\mathbf{k}\sigma l}$) creates (annihilates) a non-interacting electron in the bath with momentum $\mathbf{k}$, spin σ and dispersion relation $\epsilon_{\mathbf{k}l}$. The first term describes the kinetic energy of the electron bath. The second term includes the local energy levels ϵ_m of the impurity. Due to the third term an exchange of electrons between the impurity and the bath arises, with a hybridization $V_{\mathbf{k}lm}$. The last term corresponds to the Coulomb repulsion at the site of the impurity.

It is convenient to formulate the problem at hand in terms of functional integrals in combination with Grassmann variables Ψ and Ψ^* [58]. This in particular allows for a continuous bath (in $\hat{H}^{AIM}$ the bath degrees are discrete: $l = 1, ..., N_{bath}$).

Then one can integrate out the electrons in the bath [9] and get an effective problem with an interacting Green's function $\boldsymbol{G}^{AIM}$:

$$\boldsymbol{G}^{AIM}(i\omega_\nu) = -\frac{1}{\mathcal{Z}} \int \mathcal{D}[\psi]\mathcal{D}[\psi^*]\psi_{\sigma\nu l}\psi^*_{\sigma\nu m} e^{\mathcal{S}} \,, \tag{3.29}$$

where the index ν refers to the corresponding Matsubara frequency ω_ν and the partition function $\mathcal{Z}$ is

$$\mathcal{Z} = \int \mathcal{D}[\psi]\mathcal{D}[\psi^*] e^{\mathcal{S}} \,. \tag{3.30}$$

Here, the action $\mathcal{S}$ of this effective problem is defined via

$$\begin{aligned} \mathcal{S} = &\sum_{\nu\sigma} \psi^*_{\sigma\nu l} \mathcal{G}^0_{lm}(i\omega_\nu)^{-1} \psi_{\sigma\nu m} \\ &- \sum_{\substack{\sigma\sigma' \\ ll'mm'}} U_{ll'mm'} \int_0^\beta \psi^*_{\sigma l}(\tau)\psi_{\sigma' l'}(\tau)\psi^*_{\sigma' m}(\tau)\psi_{\sigma m'}(\tau) d\tau \,, \end{aligned} \tag{3.31}$$

where $\mathcal{G}^0$ is the non-interacting Green's function.

Self-consistent equations

The mapping of the Hubbard model in the limit of infinite dimensions onto an AIM yields a set of self-consistent equations [9]: One starts with a trial self-energy $\boldsymbol{\Sigma}$, from which we can calculate the local lattice Green's function $\boldsymbol{G}$ via [9]

$$\boldsymbol{G}(i\omega_\nu) = \sum_{\mathbf{k}} [i\omega_\nu \mathbb{1} + \mu \mathbb{1} - \boldsymbol{\epsilon}_{\mathbf{k}} - \boldsymbol{\Sigma}(i\omega_\nu)]^{-1} \,, \tag{3.32}$$

where μ is the chemical potential, $\boldsymbol{\epsilon}_{\mathbf{k}}$ is the one-particle Hamiltonian in a local basis and $\mathbb{1}$ is the identity matrix in orbital indices. Given $\boldsymbol{G}$ and $\boldsymbol{\Sigma}$, we can calculate the non-interacting Green's function of the AIM $\mathcal{G}^0$ by employing the Dyson equation

$$\boldsymbol{\mathcal{G}}^0(i\omega_\nu)^{-1} = \boldsymbol{G}(i\omega_\nu)^{-1} + \boldsymbol{\Sigma}(i\omega_\nu) \tag{3.33}$$

Subsequently, we solve the Anderson impurity model by calculating $\boldsymbol{G}^{AIM}$ via Eq. (3.29). Using Dyson's equation (Eq. (3.26)) we can then calculate the self-energy of the AIM Σ^{AIM}. This new self-energy is reinserted into Eq. (3.32) and the scheme is iterated until convergence, e.g., $\sum_\nu \left|\Sigma^{N+1}(i\omega_\nu) - \Sigma^N(i\omega_\nu)\right| < \eta$, where η is small and N denotes the current number of iterations. The DMFT loop of the self-consistent calculation is illustrated in Fig. 3.2.

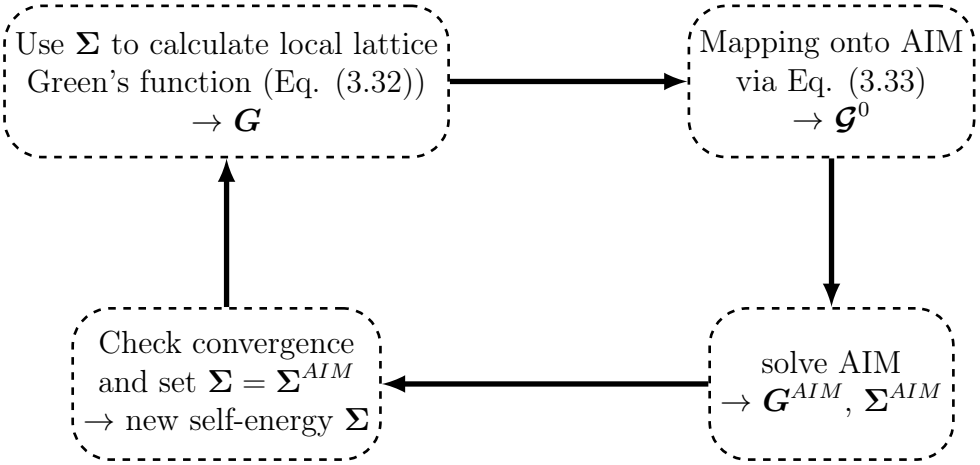

Fig. 3.2: DMFT loop of a self-consistent calculation.

3.3 DFT+DMFT

In order to perform realistic calculations for strongly correlated materials, one can combine DFT with DMFT to the so-called DFT+DMFT [11, 12] approach. In DFT+DMFT, we can treat a subset of correlated orbitals $\mathcal{C}$ in DMFT while the overall electronic structure is computed in DFT. In the case of $YIn_{1-x}Mn_xO_3$, the correlated subspace $\mathcal{C}$ refers to the $3d$ orbitals of Mn.

3.3.1 The Hamiltonian

In order to formulate a combined DFT and DMFT approach, we consider the Hamiltonian in Eq. (3.15). We start with the non-interacting H^0, which we want to extract from DFT. Following the considerations of Ref. [56], we can write the Kohn-Sham Hamiltonian in Eq. (3.3) in second quantization:

$$\hat{H}^{DFT} = \sum_{\sigma} \int \hat{\Psi}^{\dagger}_{\sigma}(\mathbf{r}) \left[-\frac{\triangle}{2} + v_{eff}(\mathbf{r}) \right] \hat{\Psi}_{\sigma}(\mathbf{r}) d^3r \,, \tag{3.34}$$

which simplifies, using the field operators in Eq. (3.14) with Wannier-functions and the Fourier transformed expression as in Eq. (3.18), to

$$\hat{H}^{DFT} = \sum_{\sigma} \sum_{iljm} t^{DFT}_{iljm} \, \hat{c}^{\dagger}_{\sigma il} \, \hat{c}_{\sigma jm} = \sum_{\sigma \mathbf{k} lm} \varepsilon^{DFT}_{\mathbf{k}lm} \, \hat{c}^{\dagger}_{\sigma \mathbf{k}l} \, \hat{c}_{\sigma \mathbf{k}m} \,. \tag{3.35}$$

Here, t^{DFT}_{imjl} and $\varepsilon^{DFT}_{\mathbf{k}ml}$ are defined by

$$\begin{aligned} t^{DFT}_{iljm} &= \int w^*_{il}(\mathbf{r}) \left[-\frac{\triangle}{2} + v_{eff}(\mathbf{r}) \right] w_{jm}(\mathbf{r})\, d^3r \text{ and} \\ \varepsilon^{DFT}_{\mathbf{k}lm} &= \frac{1}{N_L} \sum_{ij} t^{DFT}_{iljm}\, e^{i\mathbf{k}(\mathbf{R}_i - \mathbf{R}_j)}. \end{aligned} \tag{3.36}$$

Next, we consider the interacting part of the Hamiltonian. In the DFT+DMFT approach the local Coulomb interaction will only be applied to orbitals l which are in the subset of correlated orbitals $\mathcal{C}$ ($l \in \mathcal{C}$). The total Hamiltonian $\hat{H}$ can now be written as [12]

$$\hat{H} = \hat{H}^0 + \frac{1}{2} \sum_{\sigma\sigma'} \sum_{\substack{\boldsymbol{i} \\ ll'mm' \in \mathcal{C}}} U_{ll'mm'}\, \hat{c}^\dagger_{\sigma \boldsymbol{i} l}\, \hat{c}^\dagger_{\sigma' \boldsymbol{i} l'} \hat{c}_{\sigma' \boldsymbol{i} m}\, \hat{c}_{\sigma \boldsymbol{i} m'} \ . \tag{3.37}$$

Here, the onsite Coulomb interaction is only applied to orbitals l in the correlated subspace $\mathcal{C}$ ($l \in \mathcal{C}$). The rest is described by the non-interacting part $\hat{H}^0$.

We note that $\hat{H}^0 \neq \hat{H}^{DFT}$, since t^{DFT}_{iljm} and $\varepsilon^{DFT}_{\mathbf{k}lm}$ contain an effective potential $v_{eff}(\mathbf{r})$, which includes the Hartree term as well as the DFT exchange and correlation potential. Therefore, it is necessary to correct the correlation effects which are already described within DFT. Similar to the LSDA+U by V. I. Anisimov et al. [34] (see Sec. 3.1.3), we introduce a double counting term. The non-interacting part of the Hamiltonian can be approximated as [12]

$$\hat{H}^0 \approx \hat{H}^{DFT} - \hat{H}^{DC} = \sum_{\sigma \mathbf{k} lm} \varepsilon^{DFT}_{\mathbf{k}lm}\, \hat{c}^\dagger_{\sigma \mathbf{k} l}\, \hat{c}_{\sigma \mathbf{k} m} - \sum_{\substack{\boldsymbol{i}\sigma \\ l \in \mathcal{C}}} \varepsilon^{DC}\, \hat{n}_{\sigma \boldsymbol{i} l} \ , \tag{3.38}$$

where the ε^{DC} is the double-counting correction, which is applied to all correlated orbitals with $l \in \mathcal{C}$.

3.3.2 Charge self-consistent calculations

In order to perform DFT+DMFT calculations we apply a so-called fully charge self-consistent scheme, as implemented in the *TRIQS/DFTTools* [49, 59] package. We start with an initial DFT calculation, which gives us the DFT band structure $\boldsymbol{\epsilon}^{DFT}_{\mathbf{k}}$ (Eq. (3.36)) and associated Kohn-Sham orbitals. Together with the interaction matrix $U_{ll'mm'}$ and the double-counting term, this defines the many-body problem, which we solve in DMFT.

In order to set-up the DMFT calculation we need to change from the Kohn-Sham orbitals to a localized basis set. This step can be achieved by using the

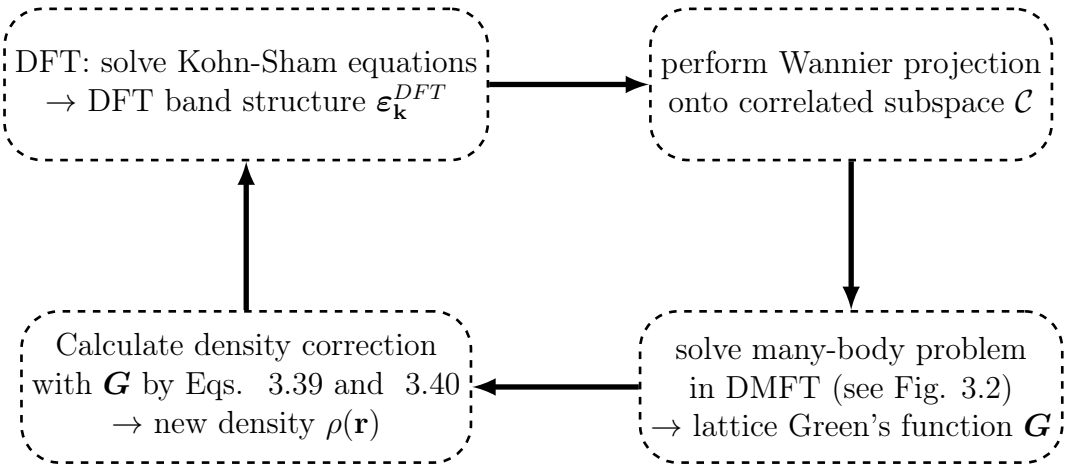

Fig. 3.3: DFT+DMFT loop of a full charge self-consistent calculation.

projective Wannier function method, as introduced in Sec. 3.1.5. The exact formalism of the projection onto the correlated subspace $\mathcal{C}$ and its implementation with *WIEN2k* Kohn-Sham orbitals can be found in Ref. [50]. The so defined impurity problem can now be solved using the self-consistent DMFT equations (see Sec. 3.2.2). This yields a lattice Green's function, from which we can calculate a density matrix via [59]

$$N_{\mathbf{k}\,nn'} = \sum_{\nu} G_{nn'}(\mathbf{k}, i\omega_\nu) e^{i\omega_\nu 0^+} \ , \tag{3.39}$$

and a new charge density, including corrections due to correlation effects, as [59]

$$\rho(\mathbf{r}) = \rho_{o\mathcal{W}}(\mathbf{r}) + \sum_{\mathbf{k}\,nn'} \langle \mathbf{r}|\psi_{n\mathbf{k}}\rangle \, N_{\mathbf{k}\,nn'} \, \langle \psi_{n'\mathbf{k}}|\mathbf{r}\rangle \ . \tag{3.40}$$

Here, n, n' denote the band indices within the projection window $\mathcal{W}$, $\psi_{n\mathbf{k}}$ are the Kohn-Sham orbitals and $\rho_{o\mathcal{W}}(\mathbf{r})$ is the density outside $\mathcal{W}$. The new updated density is again used within DFT, closing the loop. This is repeated until the density $\rho(\mathbf{r})$, as well as the self-energy Σ is converged. Fig. 3.3 illustrates the flow of the charge self-consistent DFT+DMFT calculation.

3.3.3 Hubbard-I approximation

In our calculations, we employ the Hubbard-I (H-I) approximation to solve the DMFT impurity problem. The H-I approximation was introduced by J. Hubbard in Ref. [52] and considers the problem in the atomic limit. In Ref. [12] A. I. Lichtenstein and M. I. Katsnelson further formulated this approximation in the

context of the LDA++ approach (in our notation LDA+DMFT(H-I)). In Hubbard-I, we approximate the DMFT self-energy by its quasi-atomic form

$$\mathbf{\Sigma}(i\omega) = \mathbf{\Sigma}^{at}(i\omega)\,, \tag{3.41}$$

where the Hamiltonian for the effective quasi-atomic problem reads

$$\hat{H}^{at} = \sum_{\sigma lm} \epsilon_{lm} \hat{c}^{\dagger}_{\sigma l} \hat{c}_{\sigma m} + \frac{1}{2} \sum_{\substack{\sigma\sigma' \\ ll'mm'}} U_{ll'mm'}\, \hat{c}^{\dagger}_{\sigma l}\, \hat{c}^{\dagger}_{\sigma' l'} \hat{c}_{\sigma' m}\, \hat{c}_{\sigma m'}. \tag{3.42}$$

Here, ϵ_{lm} are the quasi-atomic energies, which are a matrix in orbital indices l, m. The Hamiltonian has Eigenstates $|\mu\rangle$ with corresponding Eigenenergies E_μ. The associated atomic Green's function $\boldsymbol{G}^{at}$ is given by its Lehmann representation [55]

$$\begin{aligned} \boldsymbol{G}^{at}(i\omega) &= \frac{1}{\mathcal{Z}} \sum_{\mu\nu} \frac{\langle \mu | c_{\sigma l} | \nu \rangle \, \langle \nu | c^{\dagger}_{\sigma m} | \mu \rangle}{i\omega + E_\mu - E_\nu} (e^{-\beta E_\mu} - e^{-\beta E_\nu})\,, \text{ with} \\ \mathcal{Z} &= \sum_{\mu} e^{-\beta E_\mu}\,. \end{aligned} \tag{3.43}$$

With the non-interacting Green's functions $[\mathcal{G}^0]^{-1} = i\omega\mathbb{1} - \boldsymbol{\epsilon}$ the quasi-atomic self-energy then reads

$$\mathbf{\Sigma}^{at}(i\omega) = i\omega\, \mathbb{1} - \boldsymbol{\epsilon} - \boldsymbol{G}^{at^{-1}}\,. \tag{3.44}$$

When we compare Eq. (3.42) with the Hamiltonian of the AIM (Eq. (3.28)), we can see that the quasi-atomic H-I approximation neglects hybridization. This assumption is acceptable if the states at the impurity site are well localized and we assume that this is the case for the Mn-3*d* orbitals. However, a check of this approximation with some more advanced solver, e.g., *TRIQS/CTHYB* [48, 60], should be done. Nevertheless, in H-I, it is feasible to describe the correlation effects in a multi-orbital system even for large simulation cells, as needed in the case of $YIn_{1-x}Mn_xO_3$, at reasonable computational cost.

3.3.4 The mBJ@DFT+DMFT approach and implementation details

Although DFT+DMFT takes into account correlation effects, the part which is described by DFT still has its limitations. It has been shown that using LDA or GGA (see Sec. 3.1.2) to formulate the exchange and correlation potential, typically underestimates band gaps [61]. Therefore, it is necessary to simultaneously improve on the band gap and the correlated Mn-3*d* states.

The underestimation of the band gap could be repaired by applying the TB-mBJ potential, as described in Sec. 3.1.4. We employ the TB-mBJ potential in

a perturbative way, as proposed by H. Jiang [62], since it is not formally derived from a exchange and correlation energy functional and therefore can result in convergence problems, when used self-consistently. In this so-called mBJ@XC approach (with XC being the exchange and correlation potential) one performs a self-consistent DFT calculation and subsequently another cycle with the TB-mBJ potential [62]. This approach has shown good results for the band gaps for a wide range of semiconductors [62]. We will use this approach later on when calculating the electronic structure of $YInO_3$.

However, the description in mBJ@XC is not sufficient when considering $YIn_{1-x}Mn_xO_3$, since correlation effects in the Mn-3d orbital play a role. Therefore, we want to treat the correlation effects with DFT+DMFT, but also incorporate non-local exchange within the description of the TB-mBJ potential. The so-called mBJ@DFT+DMFT [13, 14] scheme combines the two approaches. We apply this scheme in the same way as in Refs. [13] and [14], where the starting point is a fully charge self-consistent LDA+DMFT calculation (see Fig. 3.3). Here, the DMFT impurity problem is solved with the H-I approximation (see Sec. 3.3.3). After convergence, the TB-mBJ potential is applied in a perturbative way, correcting the Kohn-Sham band structure [13]. Subsequently, we perform a Wannier projection onto the correlated subspace $\mathcal{C}$ to solve the self-consistent DMFT equations with the H-I approximation [13]. A flow diagram of the mBJ@DFT+DMFT approach is depicted in Fig. 3.4.

Analogous to Ref. [14], we employ the double-counting correction in the fully-localized limit [63]:

$$\varepsilon^{DC} = U\left(N^{at} - \frac{1}{2}\right) - J_H\left(\frac{1}{2}N^{at} - \frac{1}{2}\right), \tag{3.45}$$

with the atomic occupancy N^{at} in the correlated shell. Here, $J_H = U_{lmlm}$ is the Hund's coupling. In the case of Mn^{3+}, we have $N^{at} = 4$.

3.4 Optical properties

Since we are interested in the occurrence of the blue color in $YIn_{1-x}Mn_xO_3$, we still need to describe the methods used to calculate the optical properties. Generally, incident light will lead to a response of the material, which depends on its electronic structure. If we consider a time-dependent electric field E_β, polarized along direction $\beta = \{x, y, z\}$, the corresponding response will be an induced current J_α. The response function connecting the two quantities, is the conductivity

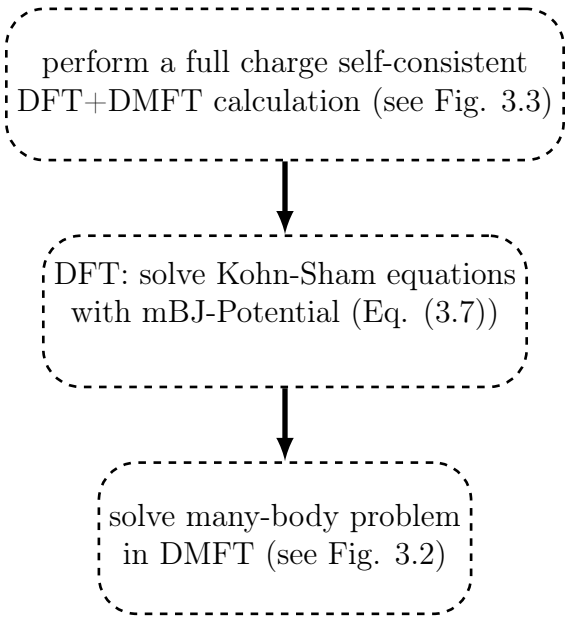

Fig. 3.4: Flow diagram of the mBJ@DFT+DMFT approach.

$\tilde{\sigma}_{\alpha\beta}$, which is defined, in linear response theory for a homogeneous system, as [64]

$$\begin{aligned} J_\alpha(\mathbf{r},t) &= \sum_\beta \tilde{\sigma}_{\alpha\beta}(\mathbf{q},\omega) E_\beta(\mathbf{r},t) \text{ , with} \\ E_\beta(\mathbf{r},t) &= E^0_\beta \, e^{i(\mathbf{q}\cdot\mathbf{r}-\omega t)} \text{ .} \end{aligned} \tag{3.46}$$

Here, E^0_β is the amplitude of the total electric field along polarization direction β.

The wavelengths of visible light are much larger than the inter-atomic distances in a solid (usually of the order of a few Å). Therefore, it is justified to neglect the momentum transfer of the incident photons ($\mathbf{q} \to 0$), which is also referred to as the dipole approximation.

The optical conductivity $\sigma_{\alpha\beta}$ can now be defined via the the real part of the conductivity within the dipole approximation, i.e. $\sigma_{\alpha\beta}(\omega) \overset{\text{def}}{=} \Re\{\tilde{\sigma}_{\alpha\beta}(\mathbf{q}=0,\omega)\}$ and can be written in SI-units, by neglecting vertex corrections, as [65]

$$\begin{aligned} \sigma_{\alpha\beta}(\Omega) = \frac{2\pi e^2\hbar}{V} \sum_{\mathbf{k}} \int d\omega \, \frac{f(\omega) - f(\omega+\Omega)}{\Omega} \\ \times \mathrm{Tr}\{v_{\alpha\mathbf{k}} \, A_{\mathbf{k}}(\omega) v_{\beta\mathbf{k}} \, A_{\mathbf{k}}(\omega+\Omega)\} \text{ ,} \end{aligned} \tag{3.47}$$

where V is the unit cell volume, $f(\omega)$ is the Fermi-function and α the polarization direction of the incident light. $v_{\alpha\mathbf{k}}$ denotes the velocities or transition matrices along α, which give the weight of the optical transition at a certain $\mathbf{k}$-point. Here,

$A_{\mathbf{k}}(\omega)$ is the **k**-resolved spectral function, obtained from mBJ@DFT+DMFT. The trace in Eq. (3.47) is taken over the orbital indices of $v_{\alpha\mathbf{k}}$ and $A_{\mathbf{k}}(\omega)$.

To analyze the optical response, we further calculate the joint density of states (JDOS), which is usually defined via the convolution of the valence and conduction-band DOS [66]. We define here a weighted joint density of states $D(\Omega)$ via

$$D(\Omega) \propto \int d\omega \, \frac{f(\omega) - f(\omega + \Omega)}{\Omega} \, A(\omega) \, A(\omega + \Omega) \, . \tag{3.48}$$

Here, $A(\omega)$ is the **k**-integrated spectral function or DOS and $f(\omega)$ is the Fermi-function. The weight of $\frac{f(\omega)-f(\omega+\Omega)}{\Omega}$ accounts for the occupation of states at finite temperature and is used in similarity to Eq. (3.47). We note that $D(\Omega)$ does not incorporate the **k**-dependent weight of the optical transition given by $v_{\alpha\mathbf{k}}$, as it is the case for the optical conductivity in Eq. (3.47). For further analysis, we can also define a partial JDOS $D_l(\Omega)$, which describes the contribution to $D(\Omega)$ arising from transitions between the orbital l. It is defined by

$$D_l(\Omega) \propto \int d\omega \, \frac{f(\omega) - f(\omega + \Omega)}{\Omega} \, A_l(\omega) \, A_l(\omega + \Omega) \, , \tag{3.49}$$

where $A_l(\omega)$ is the contribution to the **k**-integrated spectral function or DOS from the orbital l. For example, in the case of $YIn_{1-x}Mn_xO_3$, the partial JDOS of the Mn-3d orbital $D_{\text{Mn-}3d}$ will play an important role to identify transitions between d bands.

In order to compare our results of the optical conductivity with experiments, it is often practical to calculate the diffuse reflectance R. We use the approach used in Ref. [67] to calculate R, which is based on the Kubelka-Munk (KM) model [68, 69], where the propagation of two light fluxes through a film is considered. The diffuse reflectance of an infinitely thick film in the bulk limit R_∞ can be written as [67]

$$\begin{aligned} R_\infty &= \alpha - \sqrt{\alpha^2 - 1} \, , \text{ with} \\ \alpha &= 1 + \frac{2K}{\beta}. \end{aligned} \tag{3.50}$$

Here, β denotes the effective scattering parameter and K is the macroscopic absorption coefficient, which is given by [67]

$$K(\omega) = \frac{\omega}{c} \Im \left\{ \sqrt{1 + \frac{4\pi i}{\omega} \tilde{\sigma}(\omega)} \right\} , \tag{3.51}$$

where c is the speed of light, $\Im$ denotes the imaginary part and $\tilde{\sigma}$ is the complex conductivity with its real part as in Eq. (3.47).

We want to go one step further and calculate the color coordinates in the CIE 1931 XYZ color space [70, 71] , with the associated color matching functions $\bar{x}(\lambda), \bar{y}(\lambda), \bar{z}(\lambda)$. In order to do this we consider the reflectance of the material $R(\lambda)$ (Eq. (3.50)) and the relative spectral power distribution $S(\lambda)$ of the incident light to calculate the color coordinates X,Y,Z by [72]

$$\begin{aligned} \begin{pmatrix} X \\ Y \\ Z \end{pmatrix} &= k \int R(\lambda) S(\lambda) \begin{pmatrix} \bar{x}(\lambda) \\ \bar{y}(\lambda) \\ \bar{z}(\lambda) \end{pmatrix} d\lambda \quad \text{, with} \\ k &= \left(\int S(\lambda) \bar{y}(\lambda)\, d\lambda \right)^{-1} . \end{aligned} \tag{3.52}$$

Here, we use the CIE standard illuminant D65 [73] for $S(\lambda)$.

Chapter 4

Results

In this chapter, the results of the calculations for $YIn_{1-x}Mn_xO_3$ are presented. I will start the investigation with the structural relaxation in Sec. 4.1 for $YIn_{1-x}Mn_xO_3$ with different Mn-concentrations x. The relaxed structure will then be employed in the mBJ@DFT+DMFT (see Sec. 3.3.4) calculations of the electronic structure and for the computation of the optical properties in Sec. 4.2.

4.1 Structural relaxation

Besides pure $YInO_3$ and $YMnO_3$ we want to investigate the structure, especially the bond lengths within the MO_5 TBP, for low Mn-concentrations. We consider $x = 8.33\%$ and $x = 16.67\%$, since this is the regime where the blue color is reported [1]. We perform the structural relaxation, which is done within LDA and LSDA+U, in two steps. First, we extract the lattice parameters from experiments in Ref. [6] and than we optimize the internal coordinates of a supercell corresponding to the chosen doping [1]. From the final structures we extract the bond lengths of the MO_5 polyhedra.

4.1.1 Lattice parameters

In Ref. [6], the lattice parameters of $YIn_{1-x}Mn_xO_3$ have been measured for various x and the results, illustrated in Figure 2 of Ref. [6], show a linear dependence on the Mn-concentration. In order to get lattice parameters for arbitrary Mn concentrations, we perform a linear fit to the experimental data of Ref. [6]. Details of the fit are reported in Sec. A.1. Fig. 4.1 shows the results of the fits (blacked dashed line), as well as experimental values [6] (red triangles) for a (first row) and

[1] Here and in the following we only consider one unit-cell per doping. In principle, different doping sites and an averaging procedure could be performed.

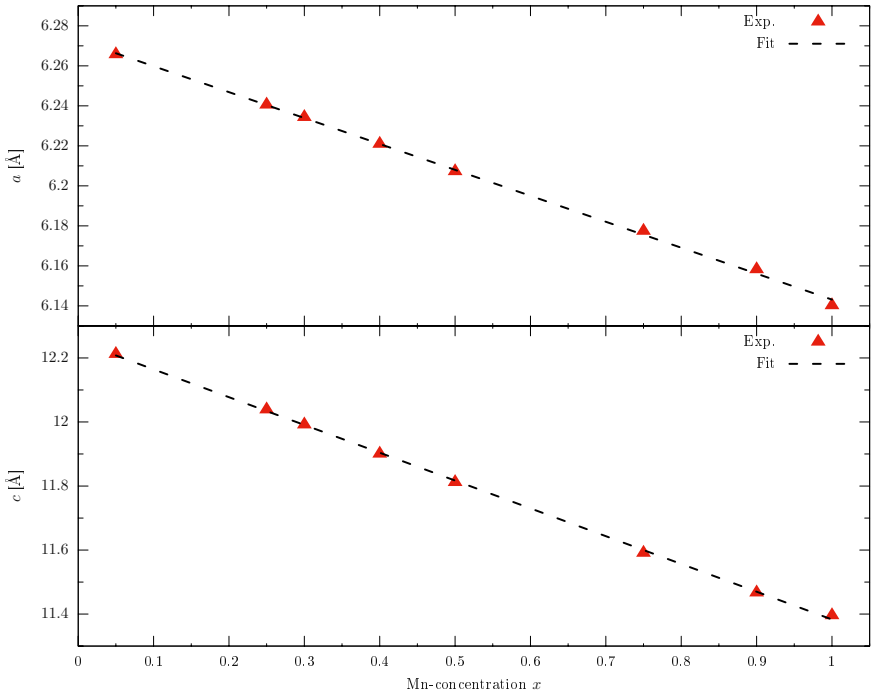

Fig. 4.1: Lattice parameters of $YIn_{1-x}Mn_xO_3$ as a function of the Mn-concentration x. Linear fit (black dashed line) to experimental data (red triangle) taken from Ref. [6]. The first row depicts the fit and experimental data for a and the second row illustrates the results for c.

c (second row). One can clearly see that the linear fit to the experimental data is accurate, making it possible to extract the lattice parameters for arbitrary Mn concentrations. Note that the observed decrease of a and c with increasing x is due to the replacement of large In^{3+} ions with smaller Mn^{3+} ions [6]. The decrease of the lattice parameters is especially pronounced in the $c-$axis and much less in a, which is reflected in a significant change of the axial bond lengths [6], as will be seen.

4.1.2 Optimization of internal coordinates and bond lengths

We can now perform the optimization of the internal coordinates for different concentrations x. We employ the *WIEN2k* [35, 36] program package for this task. Technical details can be found in Sec. A.2. We have performed the optimization of the internal coordinates within LDA, as well as LSDA+U, where the on-site Coulomb interaction is applied to the Mn-3d orbitals. The resulting bond lengths of the relaxed structures are reported in this section for each Mn-concentration

individually. An overview of In–O and Mn–O distances for all x considered here, as well as experimental data of Ref. [6] can be found in Appendix A, Table A.2 and Table A.3, respectively.

$YInO_3$

The experimental lattice parameters for pure $YInO_3$ extracted from the fit in Fig. 4.1 are $a = 6.2728$ Å and $c = 12.2511$ Å. They agree very well with further measurements in Ref. [74], where $a = 6.2727$ Å and $c = 12.2563$ Å are reported. The hexagonal structure, with space group $P6_3cm$, is depicted in Fig. 2.1.

We employ the lattice parameters a,c from the fit in Fig. 4.1 and optimize the internal parameters within LDA. This yields the relaxed structure, from which we measure the bond lengths within the In–O_5 polyhedra. The In–O distances are reported in Table 4.1. The first column reports experimental data of ℓ from Ref. [74], which was the starting point of our relaxations. The second column is ℓ taken from Ref. [6] and the third column are our theoretical the In–O distances after optimization of the internal coordinates. Theoretical and experimental values for bond lengths agree very well, in particular if one compares the values from the second and third column, which correspond to the same a and c parameters.

bond	ℓ [Å] Exp. [74]	ℓ [Å] Exp. [6]	ℓ [Å] (LDA)
axial In–O_1	2.005	2.089	2.088
axial In–O_2	2.030	2.093	2.111
equatorial In–O_3	2.105	2.097	2.130
equatorial In–O_4	2.098	2.127	2.122
equatorial In–O_5	2.098	2.127	2.122

Table 4.1: In–O bond lengths ℓ of $YInO_3$. The first column reports experimental data measured in Ref. [74]. The second column is ℓ taken from Ref. [6] and the third column are the bond lengths after optimization of the internal coordinates performed within LDA.

$YMnO_3$

We follow the same procedure as for $YInO_3$. For $YMnO_3$, Ref. [6] reports experimental $a = 6.1402$ Å and $c = 11.3956$ Å, which will be employed in the following.

For $YMnO_3$, we perform the relaxation of the internal parameters in LDA, as well as LSDA+U since correlation effects in the Mn-3d orbitals might influence

the bond lengths. I employed two sets of interaction parameters U and J, namely U_1=5 eV and J_1=0.5 eV (as reported in Ref. [1]) and U_2=10.1 eV and J_2=0.88 eV (as utilized in Ref. [75]). This way, a possible impact of these U, J parameters on the resulting bond lengths ℓ can be investigated.

Furthermore, to rule out any possible influence of the specific magnetic order assumed within LSDA+U on the calculated bond lengths, we performed LSDA+U calculations in the ferromagnetic (FM), as well as the antiferromagnetic (AFM) state, where the latter is assumed to realize ferromagnetic Mn-planes.

Analogous to $YInO_3$, we relax the structure and extract the bond lengths. Table 4.2 reports the bond lengths, where experimental data of Ref. [6] (first column) and Ref.[26] (second column), as well as FM and AFM LSDA+U calculations (third and fourth column), together with the results of the LDA calculation (fifth column) are reported. Regarding the LSDA+U calculations (performed with U=5 eV and J=0.5 eV), we can see that the magnetic ordering does not have any impact on the resulting bond lengths. Also the choice of U and J does not influence the bond lengths, as can be seen from Table 4.3, where the Mn–O distances resulting from optimization performed within (FM) LSDA+U with $U = 5$ eV, $J = 0.5$ eV (second column) and $U = 10.1$ eV, $J = 0.88$ eV (third column) are reported. We can clearly see that the bond lengths do not substantially vary as U and J are significantly increased.

bond	ℓ [Å] Exp. [6]	ℓ [Å] Exp. [26]	ℓ [Å] (LSDA+U FM)	ℓ [Å] (LSDA+U AFM)	ℓ [Å] (LDA)
axial Mn–O_1	1.848	1.856	1.867	1.867	1.856
axial Mn–O_2	1.882	1.880	1.869	1.869	1.875
equatorial Mn–O_3	1.966	2.057	2.066	2.066	2.163
equatorial Mn–O_4	2.118	2.049	2.058	2.058	2.002
equatorial Mn–O_5	2.118	2.049	2.058	2.058	2.002

Table 4.2: Mn–O bond lengths ℓ of $YMnO_3$. The first column reports experimental data taken from Table 2 of Ref. [6] and the second column is ℓ measured from the initial structure file of Ref. [25], which is based on experimental data of Ref. [26]. The third column reports the results for a ferromagnetic (FM) and the fourth column for a antiferromagnetic (AFM) LSDA+U calculation, with U=5 eV and J=0.5 eV. The last column shows the resulting ℓ after a LDA calculation.

bond	ℓ [Å] (FM:LSDA+U $U = 5$ eV, $J = 0.5$ eV)	ℓ [Å] (FM:LSDA+U $U = 10.1$ eV, $J = 0.88$ eV)
axial Mn–O_1	1.869	1.874
axial Mn–O_2	1.867	1.873
equatorial Mn–O_3	2.066	2.066
equatorial Mn–O_4	2.058	2.059
equatorial Mn–O_5	2.058	2.059

Table 4.3: Mn–O bond lengths ℓ of $YMnO_3$. The first and second columns are the bond lengths after minimization of the internal parameters for LSDA+U calculations with U=5 eV, J=0.5 eV and U=10.1 eV, J=0.88 eV, respectively.

While LDA yields Mn–O_{ax} bond lengths, which are in better agreement with experimental data of Ref. [6] than LSDA+U, we observe that the opposite is the case for the Mn–O_{eq} distances. In all, it seems that LSDA+U does not perform significantly better than LDA. Also, a good description of the axial bond lengths is presumably more important, since they change more as the Mn-concentration is increased [6].

$YIn_{0.83}Mn_{0.17}O_3$

Next, we will consider a Mn-concentration of approximately 17 % in $YIn_{1-x}Mn_xO_3$. In order to achieve this concentrations we take the unit cell of $YInO_3$ and replace one of the six In atoms with Mn, which corresponds to $x = 1/6 = 16.67\%$. For this Mn-concentration, we use the lattice parameters of the fit in Sec. 4.1.1, which are $a = 6.2512$ Å and $c = 12.1065$ Å.

Table 4.4 depicts the Mn–O bond lengths of the optimized structure. The calculations have been performed within LDA and FM LSDA+U with $U = 5$ eV and $J = 0.5$ eV, where we stress that neither magnetic ordering nor the values of U and J significantly influence the bond lengths. The Mn–O bond lengths, especially the axial ones, shrink compared to In–O distances of $YInO_3$ (see Table 4.1). When comparing bond lengths between LDA and LSDA+U calculations, one observes that the distances within the Mn–O_5 polyhedra depict an interesting effect. Within LSDA+U the Mn–O bond lengths are quite similar, while in the case of the LDA calculation the two axial Mn–O bond lengths vary significantly. This asymmetry within Mn–O_{ax} distances has been observed in experiment [6].

The In–O bond lengths do not significantly change and their values for $x =$

bond	ℓ [Å] (LDA)	ℓ [Å] (FM:LSDA+U $U = 5$ eV, $J = 0.5$ eV)
axial Mn–O_1	1.887	1.905
axial Mn–O_2	2.053	1.912
equatorial Mn–O_3	1.865	2.029
equatorial Mn–O_4	1.865	2.029
equatorial Mn–O_5	1.892	2.030

Table 4.4: Mn–O bond lengths ℓ of $YIn_{0.83}Mn_{0.17}O_3$. The first and second columns are the bond lengths after minimization of the internal parameters for LDA and LSDA+U calculations with U=5 eV, J=0.5 eV, respectively.

16.67% are reported in Appendix A, Table A.2. Note that within the relaxed structure the axial and equatorial In–O_i bond lengths vary with the distance to the Mn atom. Therefore, the reported In–O_i distances are given by an average over all In–O_i bond lengths in the cell.

$\mathbf{YIn_{0.92}Mn_{0.08}O_3}$

Since the blue color of $YIn_{1-x}Mn_xO_3$ is more brilliant for $x \leq 10\%$ [1], we further consider a lower Mn-concentration of $x = 8.33\%$. Thus, we further construct a supercell by doubling the $YInO_3$ unit cell in **c**-direction and substitute one In site with Mn, which corresponds to $x = 1/12 = 8.33\%$ (see Appendix A, Fig. A.1(a)).

We again extract the corresponding experimental lattice parameters from the fit in Sec. 4.1.1, which yields $a = 6.2620$ Å and $c = 12.1788$ Å. The optimization of the internal parameters is then performed in LDA and LSDA+U. The resulting Mn–O bond lengths are reported in Table 4.5. Although the equatorial Mn–O bond lengths of the LSDA+U calculation are in better agreement with the experimental values in Ref. [6] for $x = 5\%$, the axial Mn–O distances are not asymmetric, as it is the case for ℓ resulting from LDA calculations. As noted above, this asymmetry has been reported experimentally [6]. Therefore, in all following calculations of the electronic structure and the optical properties I use the structure relaxed in LDA.

	x= 5%	x= 8.33%	
bond	ℓ [Å] Exp.[6]	ℓ [Å] LDA	ℓ [Å] LSDA+U
axial Mn–O_1	1.879	1.891	1.910
axial Mn–O_2	2.087	2.045	1.916
equatorial Mn–O_3	1.976	1.862	2.035
equatorial Mn–O_4	1.976	1.862	2.035
equatorial Mn–O_5	2.087	1.885	2.035

Table 4.5: Mn–O bond length ℓ of $YIn_{1-x}Mn_x$ O_3 for $x = 5\%$ and 8.33%. Experimental data taken from Table 2 of Ref. [6] is reported and denoted by Exp. [6]. Results from our calculations are indicated by the corresponding energy functional, which is either LDA or LSDA+U ($U = 5$ eV and $J = 0.5$ eV).

4.2 Electronic structure and optical properties

In this section, I present the results for the electronic structure and the optical properties of $YIn_{1-x}Mn_xO_3$ computed within the the mBJ@DFT+DMFT approach (see Sec. 3.3.4). Since experimentally the most intense blue color is observed in the low Mn-concentration regime ($x \leq 10\%$) [1], I concentrate on calculations for $YIn_{0.92}Mn_{0.08}O_3$. However, before investigating $YIn_{1-x}Mn_xO_3$ for $x = 8.33\%$, it is useful to study pure $YInO_3$.

4.2.1 $YInO_3$

In order to investigate the electronic properties of $YInO_3$, I employ the relaxed structure from Sec. 4.1 and perform calculations within LDA (see Sec. 3.1.2) and mBJ@LDA (see Sec. 3.3.4). The resulting density of states (DOS) of the LDA and mBJ@LDA calculations are depicted in Fig. 4.2(a) and (b), respectively. The total DOS (gray), as well as the contribution from the O-2p (blue), Y-4d (green) and In (yellow) states are shown. The In contribution is not shown orbitally-resolved since it is small and for energies near the Fermi level (E_F) the 4d, 5s and 5p states have similar contributions.

We can clearly see from Fig. 4.2(a), that below E_F the LDA-DOS are dominated by contributions from the O-2p orbitals. Above the Fermi level we see a shallow onset from a mixture of mainly In-5s and O-2p states until for higher energies (~ 5.5 eV) the Y-4d contribution dominates the DOS. The associated band

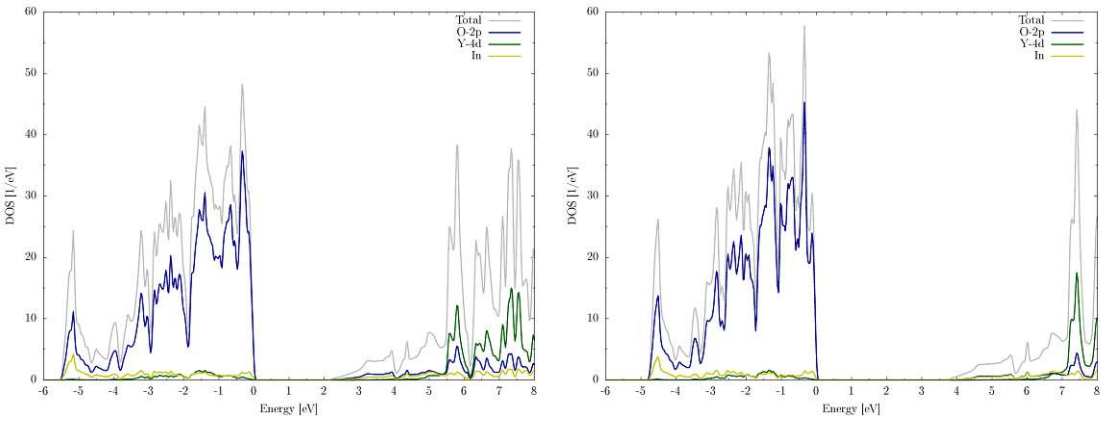

Fig. 4.2: Density of states (DOS) of $YInO_3$ within (a) LDA and (b) mBJ@LDA. The total DOS (gray) and the partial DOS arising from the O-2*p* (blue) and Y-4*d* (green) orbitals, as well as the contribution from In (yellow) are depicted.

gap for the LDA-DOS is approximately 2.1 eV. Its value is underestimated by ~ 1.6 eV compared to the apparent value of ~ 3.7 eV from the diffuse reflectance spectrum of $YInO_3$ reported in Ref. [1] (see Fig. 2.2(b)).

When we consider the mBJ@LDA-DOS in Fig. 4.2(b), we see that the main features of the electronic structure are similar to those of the LDA-DOS, but with a wider gap. In good agreement with the experimental data of Ref. [1], mBJ@LDA predicts a band gap of 3.71 eV for $YInO_3$. Thus, we conclude that the mBJ potential yields realistic band gaps for $YInO_3$ strongly suggesting that uncorrelated states in $YIn_{1-x}Mn_xO_3$ will be well captured as well.

4.2.2 $YIn_{0.92}Mn_{0.08}O_3$

In this section, I report computed spectral functions and optical conductivities for $YIn_{1-x}Mn_xO_3$ with $x = 8.33\%$. These results have been obtained by employing the mBJ@LDA+DMFT approach (see Sec. 3.3.4). Starting point for the calculations is the LDA relaxed structure (see Sec. 4.1).

The mBJ@DFT+DMFT approach step-by-step

It is instructive to study the electronic structure in every step of the calculation within the mBJ@DFT+DMFT approach, where we start with a LDA computation, followed by a fully charge self-consistent LDA+DMFT calculation before perturbatively applying the TB-mBJ potential (see Sec. 3.3.4 for more information). In this calculation, I used an energy window $\mathcal{W} = [-1\text{ eV}, 3\text{ eV}]$ around E_F for the

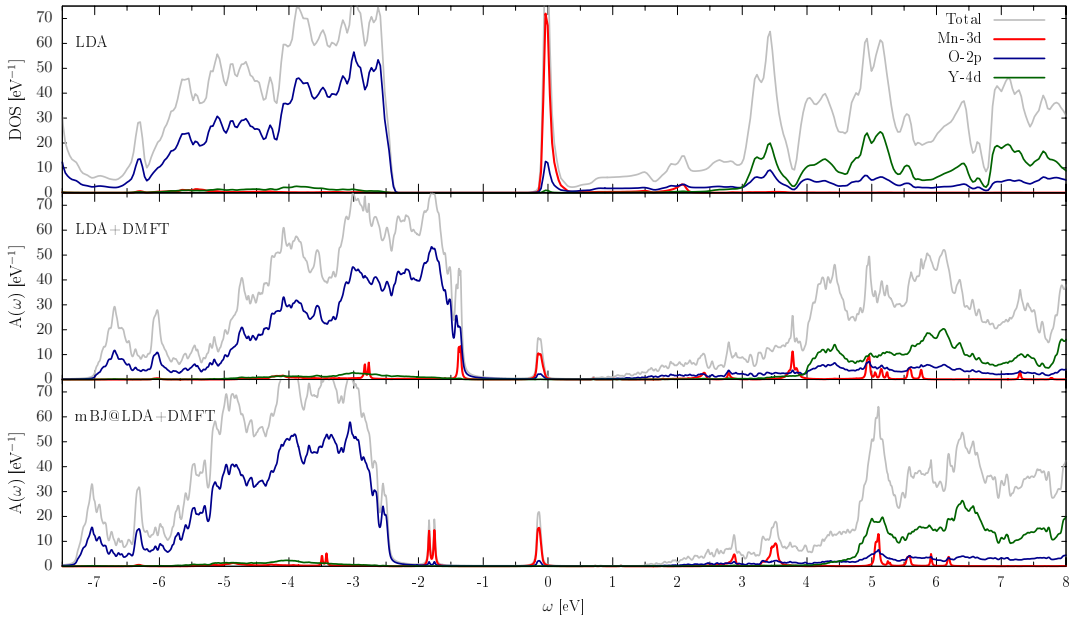

Fig. 4.3: LDA density of states (DOS) of $YIn_{0.92}Mn_{0.08}O_3$ (first row), spectral function $A(\omega)$ from LDA+DMFT (second row) and mBJ@LDA+DMFT (third row) calculations. An energy window of $\mathcal{W} = [-1\text{ eV}, 3\text{ eV}]$ around E_F was used for the Wannier projection of the correlated Mn-3d states and $U = 3$ eV, $J = 0.8$ eV. The contributions to the total DOS/$A(\omega)$ (gray) mainly originate from the O-2p (blue), the Y-4d (green) and the Mn-3d (red) states.

Wannier projection of the correlated Mn-3d states. The employed interaction parameters are $U = 3$ eV and $J = 0.8$ eV. Fig. 4.3 depicts the resulting LDA-DOS in the first row, while the second and third row show the spectral function $A(\omega)$ from LDA+DMFT and mBJ@LDA+DMFT calculations, respectively. Here, the total DOS/spectral function (gray) as well as the Mn-3d (red), O-2p (blue) and Y-4d (green) contributions are plotted. One observes that within the LDA approach a metallic state, with a large contribution of the Mn-3d states at E_F, is predicted. This is in sharp contrast to the experimentally observed optical properties of Ref. [1], and is due to the insufficient treatment of electronic correlations within LDA.

The LDA+DMFT spectral function in Fig. 4.3 shows the splitting of the Mn-3d states, due to the incorporation of correlation effects within DMFT. The Mn-3d states are split into an occupied lower and unoccupied upper Hubbard band with additional splittings due to multiplet effects and the crystal field. Note that, without the mBJ potential the gap between occupied O-2p and unoccupied In-5s hybridized with O-2p states amounts to only ~ 2 eV. As in pure $YInO_3$, we perturbatively employ the TB-mBJ potential and obtain a more reliable value of ~ 4 eV for this gap in Fig. 4.3(third row).

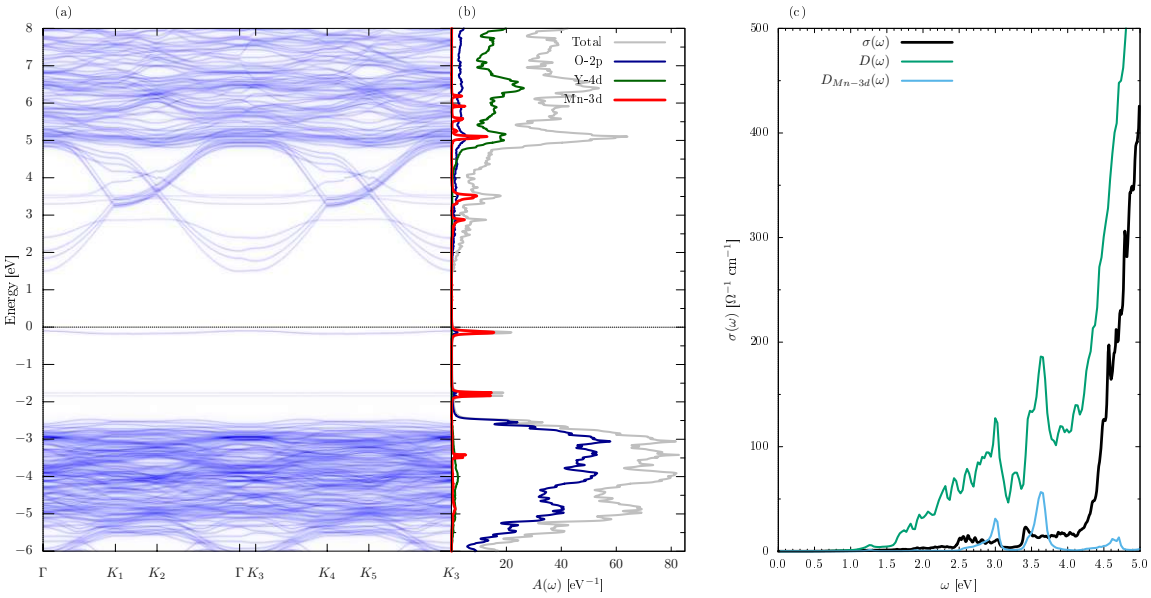

Fig. 4.4: From left to right: (a) **k**-resolved and (b) **k**-summed spectral function, as well as the (c) optical response of $YIn_{0.92}Mn_{0.08}O_3$ calculated within mBJ@LDA+DMFT. In (c), the polarization averaged optical conductivity $\sigma(\omega)$ (black), as well as the weighted JDOS $D(\omega)$ (green) and the partial JDOS of the Mn-3d states $D_{Mn-3d}(\omega)$ are depicted.

Fig. 4.4 shows the (a) **k**-resolved and (b) **k**-summed spectral function $A(\omega)$, as well as the optical response of $YIn_{0.92}Mn_{0.08}O_3$ calculated within mBJ@LDA+DMFT. Here, $A_{\mathbf{k}}(\omega)$ is calculated along the **k**-path through the Brillouin zone (BZ) specified in Appendix A, Fig. A.1(b). The optical conductivity, weighted JDOS and partial JDOS were calculated using Equations (3.47) to (3.49). We report the polarization-averaged optical conductivity, such that $\sigma(\omega) \equiv \sum_\alpha \sigma_{\alpha\alpha}(\omega)/3$. From Fig. 4.4 we can clearly see that $\sigma(\omega)$ exhibits two broad peaks in the energy range from $2-4$ eV. The first peak located from ~ 2.5 eV to ~ 3 eV and the second peak around ~ 3.4 eV. These peaks can also be seen in the weighted JDOS $D(\omega)$ and in $D_{Mn-3d}(\omega)$, where the latter suggest that these peaks mainly originate from $d-d$ transitions of unoccupied to occupied Mn-3d states. At energies > 4 eV one observes a strong increase in the optical conductivity, which can be attributed to the onset of transitions from occupied O-2p states (at ~ -2.5 eV in $A_{\mathbf{k}}(\omega)$) to the lowest unoccupied bands (at ~ 1.5 eV in $A_{\mathbf{k}}(\omega)$), consisting mainly of contributions from In-5s hybridized with O-2p states.

The effect of the Hubbard-U

Since the Hubbard U, which quantifies the strength of correlations in the Mn-3d shell is a parameter in our calculations, we want to study the changes in the electronic structure, due to a variation of U. Note that an attempt was made to calculate U from first principles using the methodology of Ref. [28], which was unsuccessful due to convergence problems in the large simulation cell and therefore we treat U as a parameter, but investigate its effects. Furthermore, the Hund's rule exchange parameter J is assumed to be 0.8 eV in all our calculations within mBJ@DFT+DMFT, which is close to the atomic value and justified since J does not dependent so much on the crystalline environment as U. Furthermore, this value for J is similar to the ones used in other works [75] investigating hexagonal $YMnO_3$.

Fig. 4.5(a)-(c) depicts the spectral function (left) and the optical properties (right) for $U = 2.5, 3, 5$ eV. One observes that the main effects of a different U value is the amount of the splitting between occupied lower and unoccupied upper Hubbard bands. Additionally, the position of the Mn-3d states relative to the uncorrelated states changes, since U enters the double-counting formula in Eq. (3.45) high-lighting that double-counting corrections are necessarily approximate.

The change of the electronic structure due to a variation of U clearly also leads to a modification of the optical properties. As it can be seen from Fig. 4.5 (a)-(c), only for $U = 2.5, 3$ eV a two peak structure can be seen in the optical conductivity. The weighted JDOS and partial JDOS indicate that these features arise from $d-d$ transitions. One observes a rigid shift of the two-peak structure to higher energies with increasing U. For the calculation with $U = 5$ eV, the unoccupied Mn-3d states are shifted to energies ≥ 4.8 eV. Therefore the $d - d$ transitions in the optical conductivity are hidden by dominating optical transitions involving O-2p and In-5s states. It is unlikely that the on-site interaction in the Mn-3d shell is as large as 5 eV, since $d - d$ transitions are expected to play an important role for the blue coloration of $YIn_{1-x}Mn_xO_3$. The value of U =2.5-3 eV on the other hand seems low for a Mn oxide. A possible role could also be played by the neglect of hybridization effects within the Hubbard-I approximation. Ref. [13] compared results from DMFT calculations using a continuous-time quantum Monte Carlo hybridization expansion solver [48, 76, 60] (CTQMC), as well as a Hubbard-I solver and observed that due to hybridization effects the Hubbard bands were shifted. This can be effectively included within Hubbard-I by a renormalization of U [13]. Considering this, one might expect that hybridization effects between O-2p and Mn-3d states could shift the occupied lower Hubbard band (Mn-3d states in the gap) to higher energies, decreasing the distance between occupied and unoccupied Mn-3d states. In principle, this could be checked by employing the CTQMC solver, which includes hybridization effects, but this is beyond the scope of this work and

we will use the Hubbard-I approximation with effective lower U-values.

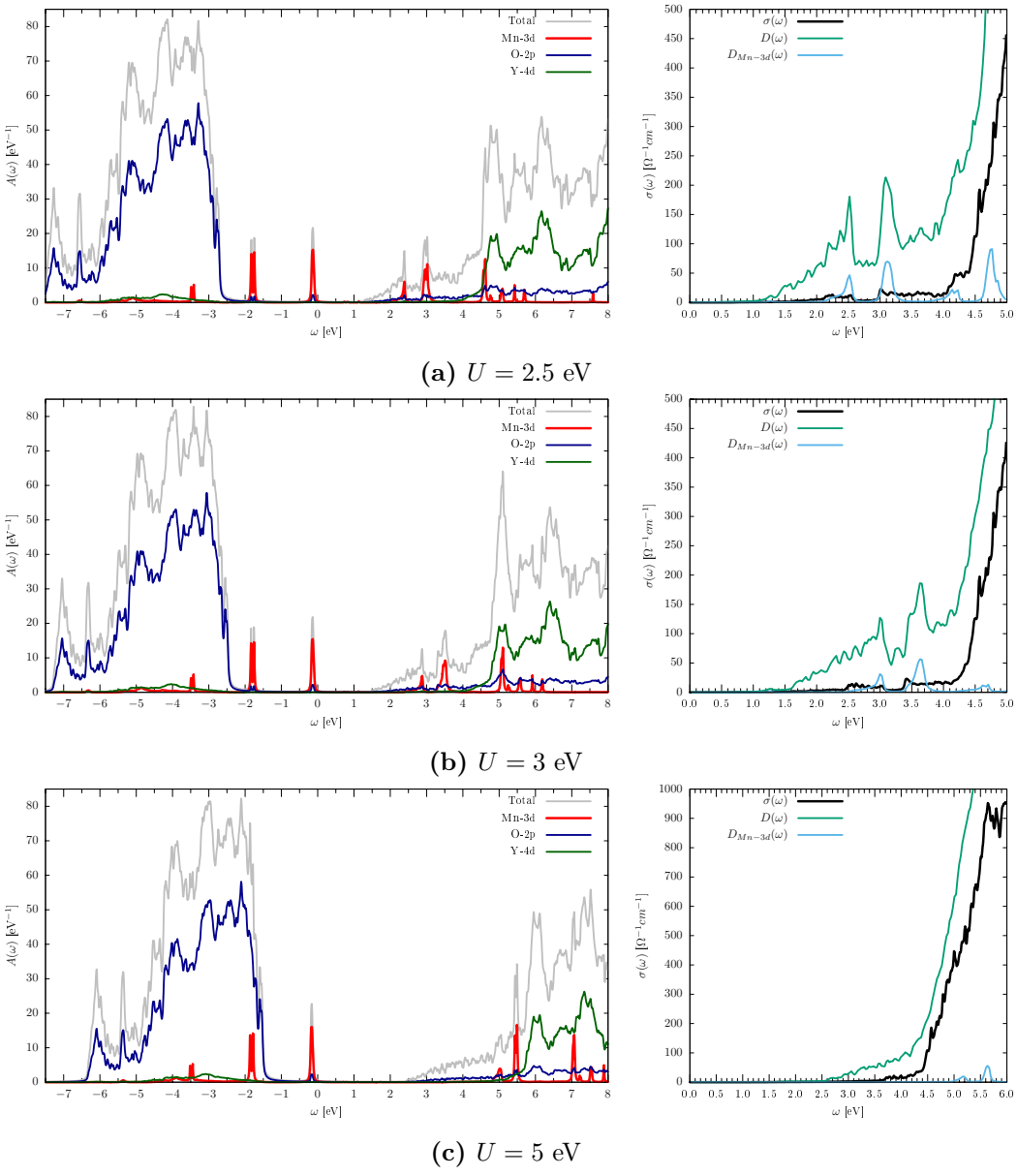

(a) $U = 2.5$ eV

(b) $U = 3$ eV

(c) $U = 5$ eV

Fig. 4.5: **k**-summed spectral function $A(\omega)$ (left) and optical properties (right) of $YIn_{0.92}Mn_{0.08}O_3$ calculated within mBJ@LDA+DMFT for $U = 2.5eV$ (a), $U = 3$ eV (b) and $U = 5$ eV (c). The contributions to the total DOS (gray) mainly originate from the O-2p (blue), the Y-4d (green) and the Mn-3d (red) orbital. For the optical properties, the polarization averaged optical conductivity $\sigma(\omega)$ (black), as well as the weighted JDOS $D(\omega)$ (green) and the partial JDOS of the Mn-3d states $D_{Mn-3d}(\omega)$ are depicted, where the latter two are plotted in arbitrary units.

The effect of the bond lengths

As described in Sec. 4.1.2 for $x = 8.33\%$, the LDA structure depicts asymmetric Mn_{ax}–O bond lengths, while a relaxation within LSDA+U leads to symmetric axial Mn–O distances (see Table 4.5). According to Ref. [6], this asymmetry within the axial Mn–O bond lengths is relevant for the blue color, so that we have taken the LDA relaxed structure in the calculations so far. Nevertheless, it is instructive to perform mBJ@LDA+DMFT calculations for a structure with symmetric bond lengths to investigate the effect of the symmetry within the axial Mn–O distances on the electronic structure and optical properties. For these calculations we use the structure relaxed within LSDA+U.

Fig. 4.6 depicts the (a) **k**-resolved and (b) **k**-summed spectral function, as well as the (c) optical response from mBJ@LDA+DMFT calculations, using $U = 2.5$ eV and $J = 0.8$ eV, for structures relaxed within (I) LDA and (II) LSDA+U. From (I) we can clearly see that the optical conductivity depicts a two peak structure, which is in agreement with the experimental data [1]. The first peak ranges from $\sim$ 2 eV to $\sim$ 2.5 eV, while the second one appears for $\simeq$ 3 eV. The weighted JDOS $D(\omega)$ (green), as well as the partial JDOS of the Mn–3d states $D(\omega)_{Mn-3d}$ indicate that both peaks bear the signature of $d-d$ transitions. If one considers the **k**-resolved spectral function in (Ia), the two-peak structure can be assigned to the $d-d$ transitions between the highest occupied Mn-3d band to the lowest ($\sim 2-2.5$ eV) and second lowest Mn-3d bands ($\sim$ 3 eV).

Considering the structure with symmetric bond lengths in Fig. 4.6(II), we observe that the first peak in the optical conductivity is shifted to higher energies of $\sim 2.3-2.8$ eV. This is due to the different local environment of the Mn^{3+} ions within the TBP, which lead to a different crystal field splitting of the Mn-3d states. This effect of the symmetric bond lengths on the electronic structure can also be seen in the spectral function.

Furthermore, one notices that the second peak disappears in the optical conductivity, even though $D(\omega)$ and $D_{Mn-3d}(\omega)$ would suggest a peak around $\sim$ 3.5 eV. Note that the main difference between the JDOS and the optical conductivity stems from the transition matrices $v_{\alpha\mathbf{k}}$ (see Eq. (3.47)). Generally speaking, one would expect atomic selection rules for transitions between totally flat bands. In this case dipole $d-d$ transitions are forbidden and the corresponding transition matrix element is zero. We assign the disappearance of the second peak in the optical conductivity, despite being present in $D(\omega)$ and $D_{Mn-3d}(\omega)$, to such a case. This is supported by the inspection of the spectral function, where one observes that two bands consisting mainly of Mn-3d states are present in low-energy unoccupied regime. One flat band at $\sim$ 2.3 eV and another more dispersive band at $\gtrsim$ 1.1 eV. The transitions between the highest occupied band at ~ -1.2 eV to the unoccupied flat band at 2.3 eV would correspond to a case, where the atomic

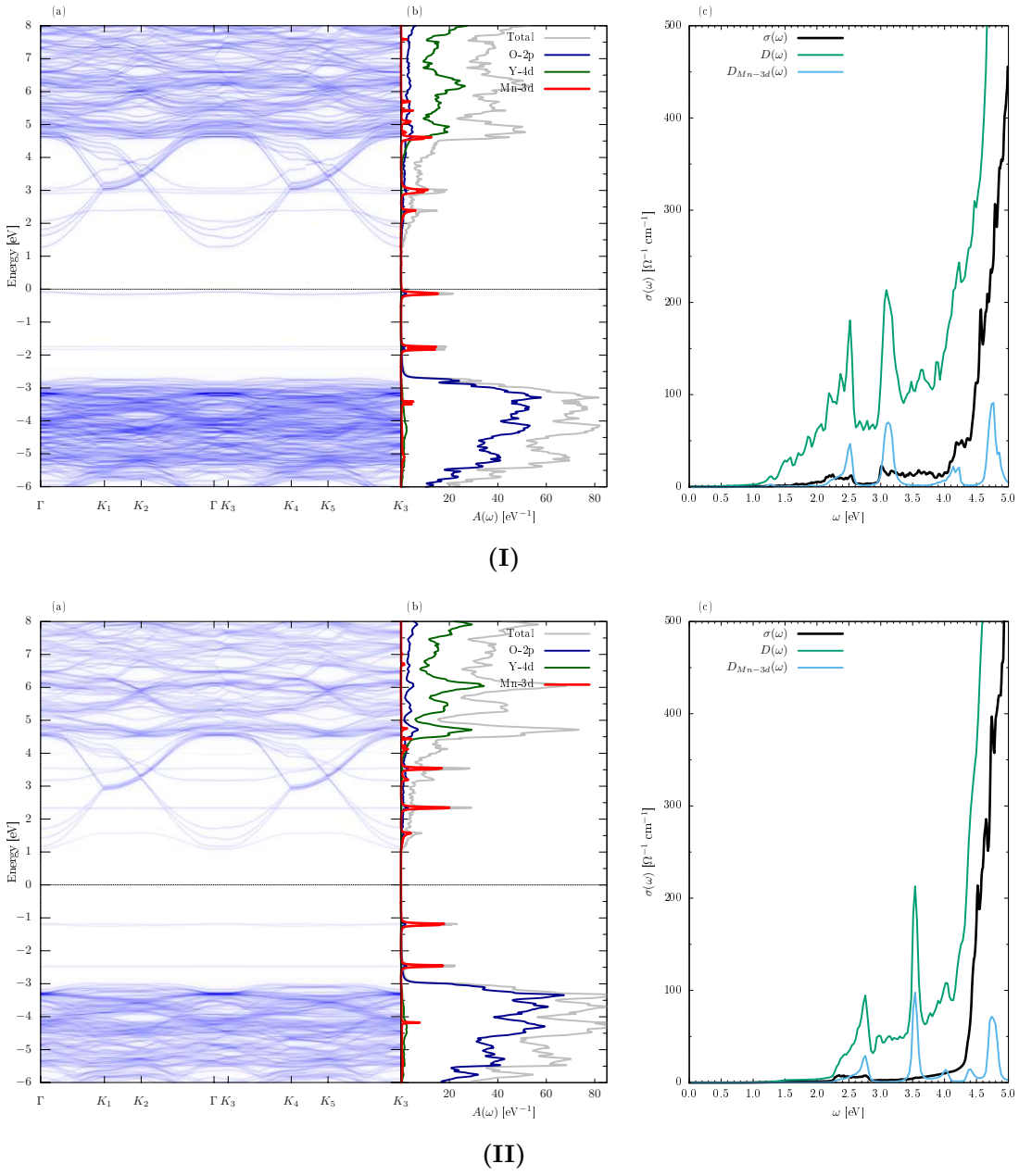

Fig. 4.6: (a) **k**-resolved and (b) **k**-summed spectral function, as well as the (c) optical response of $YIn_{0.92}Mn_{0.08}O_3$. Calculations were performed within mBJ@LDA+DMFT ($U = 2.5$ eV, $J = 0.8$ eV) for structures relaxed within (I) LDA and (II) LSDA+U. In (c), the polarization averaged optical conductivity $\sigma(\omega)$ (black), as well as the weighted JDOS $D(\omega)$ (green) and the partial JDOS of the Mn-3d states $D_{Mn-3d}(\omega)$ are depicted.

selection rules apply. Therefore, explaining why the peak at ~ 3.5 eV is observed in the JDOS, but not in the optical conductivity. Note that the second unoccupied d-band is more flat in the case of symmetric axial Mn bond lengths compared to asymmetric ones (see Fig. 4.6 (Ia) and (IIa)).

Concerning the transitions between the highest occupied Mn-3d states and the unoccupied dispersive band, $D(\omega)$ and $D_{Mn-3d}(\omega)$ show a rather asymmetric peak around $\sim 2.3 - 2.8$ eV, while the optical conductivity $\sigma(\omega)$ depicts a rather symmetric flat peak. We can understand this difference better by following the same train of thought as above. The peak in the JDOS consists of a sharp contribution at ~ 2.8 eV, arising from transitions between the flat Mn-3d band at ~ -1.2 eV to the unoccupied band at ~ 1.6 eV, which is flat in this region and dominated by contributions from Mn-3d states. This contribution from transitions between flat bands is partially suppressed in $\sigma(\omega)$ (likely by matrix element "velocity" effects). On the other side, the conduction band is more dispersive around the Γ-point and the corresponding contributions in the optical conductivity for $\omega \gtrsim 2.2$ eV gain weight relative to the transitions between flat bands. The resulting peak in $\sigma(\omega)$ is more symmetric and flat as the one in the JDOS. Note that this effect can also be seen in the optical conductivity and JDOS of the LDA relaxed structure with asymmetric bond lengths in Fig. 4.6 (Ic).

We conclude that symmetric Mn_{ax}–O bond lengths lead to the disappearance of the two-peak structure in the optical conductivity, which most likely can be understood in terms of small or even vanishing transition matrix elements (cf. atomic selection rules). This underlines the importance of the asymmetric axial Mn–O distances for the blue coloration of $YIn_{0.92}Mn_{0.08}O_3$. Therefore, we will use the corresponding structures exhibiting this asymmetry in the following calculations.

Diffuse reflectance spectra and color coordinates

We compute the diffuse reflectance, as in Eq. (3.50), using the optical conductivity calculated within mBJ@LDA+DMFT. For the computation of the diffuse reflectance, we assume that the energy dependence of the scattering parameter β is negligible in the optical range, as used previously in Ref. [67].

The resulting diffuse reflectance as a function of wavelength, $R(\lambda)$, assuming $\beta = 500$ [mm^{-1}], is depicted in Fig. 4.7. Here, the green and yellow line illustrate the calculated $R(\lambda)$ of $YIn_{0.92}Mn_{0.08}O_3$ for $U = 2.5$ and 3 eV, respectively. Experimental data for $x = 0.05$ of the diffuse reflectance was taken from Figure 8 of Ref. [5] and is plotted in blue. We can clearly see a peak for low wavelengths, where only the calculation with $U = 2.5$ eV matches the peak position, at $\lambda \sim 450$ nm, of the experiment [5]. Furthermore, our calculations for $U = 2.5$ eV shows that the diffuse reflectance begins to increase again at $\lambda \gtrsim 600$ nm, which seems to be in slight contrast to the experimental data of Ref. [5], where the rise in $R(\lambda)$ begins

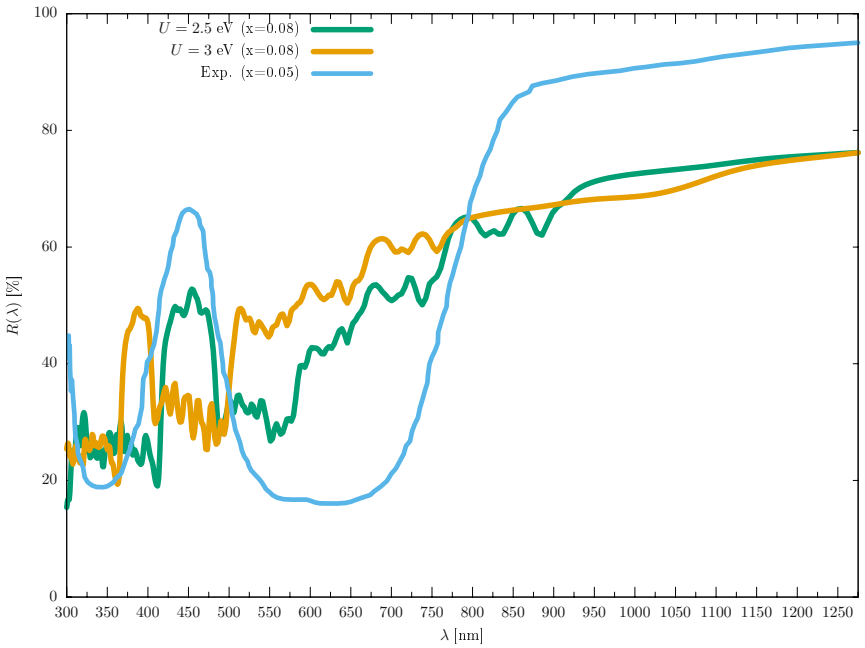

Fig. 4.7: Diffuse reflectance R of $YIn_{1-x}Mn_xO_3$ as a function of wavelengths λ. The results of the calculations within mBJ@LDA+DMFT for $x = 0.08$ and $U = 2.5eV$ (green), as well as $U = 3$ eV (yellow) are depicted. Experimental data taken from Figure 8 of Ref. [5] is illustrated in blue for a Mn-concentration of 5 %.

at ~ 700 nm. The occurrence of too much reflectivity corresponds to not enough absorbance in the low-energy region ($\omega \lesssim 2$ eV) at the onset of the first peak in $\sigma(\omega)$ (see Fig. 4.6 (Ic)). Overall, the diffuse reflectance in Fig. 4.7 is in qualitative good agreement with the experiment [5].

Next, we calculate the color coordinates as in Eq. (3.52) and transform the X, Y, Z values to the sRGB color space [77]. Since the input for the calculation of the color coordinates is the reflectance, which depends on β, also the resulting R, G, B values will depend on the scattering parameter. Fig. 4.8 (a) depicts the calculated diffuse reflectance $R(\lambda)$ for $x = 0.08$ and $U = 2.5$ eV, as well as for different values of the scattering parameter β. One observes that with increasing β also $R(\lambda)$ is increased, while the overall structure does not significantly change. Fig. 4.8 (b) illustrates the associated $R, G, B \in [0, 255]$ color coordinates as a function of β with $[0, 0, 0]$ and $[255, 255, 255]$ being black and white, respectively. Here, the values of all color coordinates rise as β is increased. The results clearly show that the B-values dominate over the entire β-range, while R and G depict similar values with a slightly greater red component.

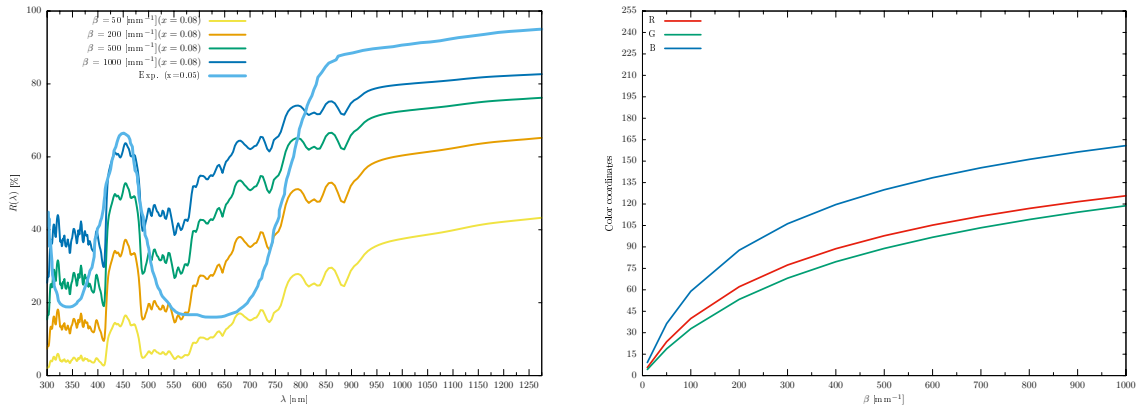

(a) **(b)**

Fig. 4.8: (a) Diffuse reflectance R of $YIn_{1-x}Mn_xO_3$ as a function of wavelength λ. The results of the calculations within mBJ@LDA+DMFT for $x = 0.08$, $U = 2.5$ eV, as well as scattering parameter $\beta = 50, 100, 200, 500, 1000$ [mm^{-1}] are depicted in yellow, dark yellow, green and dark blue, respectively. Experimental data taken from Figure 8 of Ref. [5] is illustrated in blue for a Mn-concentration of 5 %. (b) Resulting calculated color coordinates as a function of β.

Chapter 5

Conclusion

In this work, I have studied the lattice and electronic structure, as well as the optical properties of $YIn_{1-x}Mn_xO_3$, which shows a brilliant blue color for Mn-concentrations $x \lesssim 10\%$ [1]. I started by relaxing the lattice structure for $x = 0, 0.08, 0.17, 1$, within LDA [8] and LSDA+U [33, 34]. The resulting M–O bond lengths within the trigonal bipyramids (TBP), can be divided into equatorial and axial distances. Experimental data [6] depicts a certain asymmetry within the Mn_{ax}–O bond lengths (one significantly shorter than the other), which is reproduced by optimizations performed within LDA. Therefore, the LDA relaxed structure with asymmetric axial Mn–O bond lengths was employed in all further investigations.

Since the blue coloration within this compound is found for low Mn-concentrations x [1], the electronic and optical properties were computed for $x = 0$ and 0.08. For pure $YInO_3$, the mBJ@LDA approach yielded a band gap of approximately 3.71 eV, in good agreement with the experimental measurements of Ref. [1].

The investigation of $YIn_{0.92}Mn_{0.08}O_3$ was performed within mBJ@DFT+DMFT [13, 14], where the Hubbard-I [52] approximation is employed to solve the DMFT impurity problem. The resulting optical conductivity shows a two peak structure, which is also observed experimentally [1]. The comparison between the optical conductivity and the (partial) weighted joint-density of states (JDOS) reveals that for both peaks the main contribution originates from $d - d$ transitions between Mn-3d states. Note that also the optical conductivity for the structure with symmetric bond lengths (relaxed within LSDA+U) was performed. In this case, the characteristic two peak structure is not visible in the optical conductivity. This underlines the importance of the asymmetric bond lengths for the blue coloration as suggested by experimental findings in Ref. [6].

The optical conductivity were calculated for $U = 2.5$ and 3 eV. For $U = 2.5$ eV, the peak position of the diffuse reflectance R is in very good agreement with the

experimental data of Ref. [5]. Instead, in a calculation using $U = 3$ eV, the peak is slightly shifted. Note that despite the good agreement regarding the peak position, for longer wavelengths the reflectance increases too soon again compared to the experimental data [5]. Subsequently, we calculate the associated color coordinates using R computed for different values of the scattering parameter β. The results clearly depict a dominating blue contribution to the color over the entire β-range. This finding supports that our electronic structure calculations capture the essence of the physics of $YIn_{1-x}Mn_xO_3$.

We conclude that our *ab initio* calculations within mBJ@DFT+DMFT yield important insights into the electronic structure and optical transitions responsible for the blue color. Our results are further in overall good agreement with the experimental findings of Ref. [1, 5, 6]. What could be checked in the future are potential hybridization effects of the Mn-3d states. The latter are neglected in Hubbard-I, but could be investigated by employing the full *TRIQS/CTHYB* [48, 60] solver. Furthermore, it would be desirable to calculate the Hubbard-U from first principle. Nevertheless, the results presented in this work shed light on the mechanism responsible for the blue color of $YIn_{1-x}Mn_xO_3$ and suggest that a similar investigation might also be applicable to other pigment materials in the color circle of Fig. 2.3.

Appendix A

Details about the structure relaxation

A.1 Fit of the lattice parameters

For both a and c, we perform a least squares polynomial fit to the experimental data reported in Table S1 of the Supporting Information of Ref. [6], which are given in Table A.1. The function f used in the fit is linear: $f(x) = \alpha\, x + \beta$. This results in a slope α of -0.1297 Å/x and an offset β of 6.2728 Å for a. For the lattice parameter c the linear fit gives us $\alpha = -0.8682$ Å/x and $\beta = 12.2511$ Å.

x	0.05	0.25	0.3	0.4	0.5	0.75	0.9	1
a [Å]	6.2657	6.2405	6.2343	6.2209	6.2072	6.1774	6.1582	6.1402
c [Å]	12.2118	12.0385	11.9914	11.9003	11.8116	11.5905	11.4667	11.3956

Table A.1: Lattice parameter a and c for $YIn_{1-x}Mn_xO_3$. Table adapted from Table S1 of the Supporting Information of Ref. [6].

A.2 Optimization notes and bond lengths overview

The minimization of the internal coordinates is performed within *WIEN2k* [35, 36]. For more information about the structure optimization and convergence of the self-consistent field (SCF) cycle, we refer the reader to the *WIEN2k* User's Guide [78]. The number of basis functions considered is determined by the parameter $R_{MT}K_{max}$ and we use in our calculations $R_{MT}K_{max} = 6.5$. Furthermore, we

minimize the internal coordinates using 100 **k**-points in the reducible Brillouin zone and convergence criteria for the SCF-cycles, where a force convergence of 0.25 mRy/au, a energy convergence of 0.00001 Ry and a charge convergence of 0.001 e is enforced. The structure was relaxed until all forces were below 1 mRy/au. The simulation cell for $YIn_{0.92}Mn_{0.08}O_3$ (supercell with 60 atoms) is depicted in Fig. A.1(a).

An overview of all In–O and Mn–O bond lengths of $YIn_{1-x}Mn_xO_3$ for various Mn-concentrations x is given in Tables A.2 and A.3, respectively. Here, the M–O distances resulting from our calculations are marked by the DFT-functional used during the computation, which is either LDA or LSDA+U. Experimental data from Table 2 of Ref. [6] is denoted by Exp. [6].

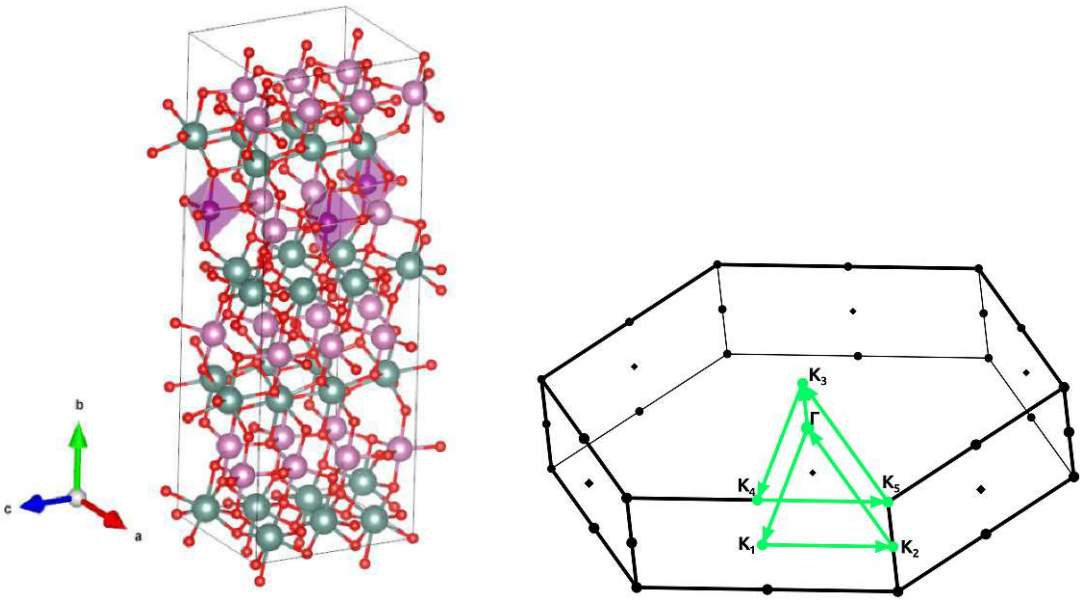

(a) **(b)**

Fig. A.1: (a) Simulation cell of $YIn_{0.83}Mn_{0.17}O_3$, relaxed within LDA, plotted in *Vesta* [24]. O (red), Y (green), In (light purple) and Mn (dark purple) atoms, as well as the bond lengths between atoms and the $Mn–O_5$ TBP are illustrated. (b) Primitive Brillouin zone (BZ) of $YIn_{0.92}Mn_{0.08}O_3$ plotted in *XCrySDen* [79]. The **k**-path through the BZ ($\Gamma - K_1 - K_2 - \Gamma - K_3 - K_4 - K_5 - K_3$) is marked by green arrows.

	x = 0		x = 5%	x = 8.3%		x = 16.6%		x = 90%
bond	ℓ [Å] Exp.[6]	ℓ [Å] LDA	ℓ [Å] Exp.[6]	ℓ [Å] LDA	ℓ [Å] LSDA+U	ℓ [Å] LDA	ℓ [Å] LSDA+U	ℓ [Å] Exp.[6]
axial In–O_1	2.089	2.088	2.086	2.080	2.085	2.070	2.080	2.078
axial In–O_2	2.093	2.111	2.090	2.103	2.106	2.093	2.100	2.083
equatorial In–O_3	2.097	2.130	2.098	2.140	2.124	2.161	2.127	2.087
equatorial In–O_4	2.127	2.122	2.121	2.144	2.125	2.168	2.129	2.116
equatorial In–O_5	2.127	2.122	2.121	2.150	2.133	2.171	2.137	2.116

Table A.2: In–O bond length ℓ of $YIn_{1-x}Mn_xO_3$ for various x. Experimental data taken from Table 2 of Ref. [6] is reported and denoted by Exp. [6]. Results from our calculations are indicated by the corresponding energy functional, which is either LDA or LSDA+U ($U = 5$ eV and $J = 0.5$ eV).

	x= 5%	x= 8.3%		x = 16.6%		x = 1		
bond	ℓ [Å] Exp.[6]	ℓ [Å] LDA	ℓ [Å] LSDA+U	ℓ [Å] LDA	ℓ [Å]) LSDA+U	ℓ [Å] Exp.[6]	ℓ [Å] LDA	ℓ [Å] LSDA+U
axial Mn–O_1	1.879	1.891	1.910	1.887	1.905	1.848	1.856	1.867
axial Mn–O_2	2.087	2.045	1.916	2.053	1.912	1.882	1.875	1.869
equatorial Mn–O_3	1.976	1.862	2.035	1.865	2.029	1.966	2.163	2.066
equatorial Mn–O_4	1.976	1.862	2.035	1.865	2.029	2.118	2.002	2.058
equatorial Mn–O_5	2.087	1.885	2.035	1 .892	2.030	2.118	2.002	2.058

Table A.3: Mn–O bond length ℓ of $YIn_{1-x}Mn_xO_3$ for various x. Experimental data taken from Table 2 of Ref. [6] is reported and denoted by Exp. [6]. Results from our calculations are indicated by the corresponding energy functional, which is either LDA or LSDA+U ($U = 5$ eV and $J = 0.5$ eV).

Appendix B

Details about electronic structure and optic calculations

B.1 Performing mBJ@DFt+DMFT calculations

The mBJ@DFT+DMFT method is performed using the *WIEN2k* [36, 35] and *TRIQS/DFTTools* [48, 49] package. For the sake of faster convergence, we start our approach with a simple LDA calculation, using 50 **k**-points in the reducible Brillouin zone and a charge convergence of 0.0001 e. Subsequently, we perform a fully charge self-consistent LDA+DMFT calculation, with an energy convergence of 0.00001 Ry for the density and a tolerance of 0.0001 for the self-energy within the Hubbard-I solver. We treat the Mn-3d states within the energy window $\mathcal{W} = [-1\text{ eV}, 3\text{ eV}]$ as correlated. On top of the LDA+DMFT calculation, we carry out one more cycle with the TB-mBJ potential and run the DMFT cycle until the self-energy, with a tolerance of 0.0001, is converged. All DMFT calculations are performed using an inverse temperature of $\beta = 40\text{ eV}^{-1}$, which correspond approximately to room temperature.

B.2 Post-processing

After we successfully converged the mBJ@LDA+DMFT calculations, we can calculate the density of states (DOS), the **k**-dependent spectral function $A_{\mathbf{k}}(\omega)$ or the optical conductivity, as implemented in the *TRIQS/DFTTools* [48, 49] package. Note that for the optical conductivity we need a denser **k**-grid and we use 1000 **k**-points in the reducible Brillouin zone (BZ) to calculate it. Concerning $A_{\mathbf{k}}(\omega)$ we choose the **k**-path through the BZ as shown in Appendix A, Fig. A.1(b) using 480 **k**-points.

List of Figures

List of Tables

Bibliography

[1] A. E. Smith, H. Mizoguchi, K. Delaney, N. A. Spaldin, A. W. Sleight, and M. A. Subramanian. „Mn^{3+} in Trigonal Bipyramidal Coordination: A New Blue Chromophore“. In: *Journal of the American Chemical Society* 131.47 (2009). PMID: 19899792, pp. 17084–17086. DOI: 10.1021/ja9080666. eprint: https://doi.org/10.1021/ja9080666. URL: https://doi.org/10.1021/ja9080666.

[2] Oregon State University. *The Story of YInMn Blue*. URL: https://chemistry.oregonstate.edu/content/story-yinmn-blue (visited on 03/09/2022).

[3] A. E. Smith, A. W. Sleight, and M. Subramanian. „Synthesis and properties of solid solutions of hexagonal $YCu_{0.5}Ti_{0.5}O_3$ with YMO_3 (M=Mn, Cr, Fe, Al, Ga, and In)“. In: *Materials Research Bulletin* 46.1 (2011), pp. 1–5. ISSN: 0025-5408. DOI: https://doi.org/10.1016/j.materresbull.2010.10.006. URL: https://www.sciencedirect.com/science/article/pii/S002554081000406X.

[4] P. Jiang, J. Li, A. W. Sleight, and M. A. Subramanian. „New Oxides Showing an Intense Orange Color Based on Fe^{3+} in Trigonal-Bipyramidal Coordination“. In: *Inorganic Chemistry* 50.13 (2011). PMID: 21627150, pp. 5858–5860. DOI: 10.1021/ic200535c. eprint: https://doi.org/10.1021/ic200535c. URL: https://doi.org/10.1021/ic200535c.

[5] J. Li, S. Lorger, J. K. Stalick, A. W. Sleight, and M. A. Subramanian. „From Serendipity to Rational Design: Tuning the Blue Trigonal Bipyramidal Mn^{3+} Chromophore to Violet and Purple through Application of Chemical Pressure“. In: *Inorganic Chemistry* 55.19 (2016). PMID: 27622607, pp. 9798–9804. DOI: 10.1021/acs.inorgchem.6b01639. eprint: https://doi.org/10.1021/acs.inorgchem.6b01639. URL: https://doi.org/10.1021/acs.inorgchem.6b01639.

[6] S. Mukherjee, H. Ganegoda, A. Kumar, S. Pal, C. U. Segre, and D. D. Sarma. „Evolution of the Local Structure within Chromophoric Mn–O_5 Trigonal Bipyramids in $YMn_{1-x}In_xO_3$ with Composition“. In: *Inorganic Chem-*

istry 57.15 (2018). PMID: 30036043, pp. 9012–9019. DOI: 10.1021/acs.inorgchem.8b00997. eprint: https://doi.org/10.1021/acs.inorgchem.8b00997. URL: https://doi.org/10.1021/acs.inorgchem.8b00997.

[7] P. Hohenberg and W. Kohn. „Inhomogeneous Electron Gas“. In: *Phys. Rev.* 136 (3B 1964), B864–B871. DOI: 10.1103/PhysRev.136.B864. URL: https://link.aps.org/doi/10.1103/PhysRev.136.B864.

[8] W. Kohn and L. J. Sham. „Self-Consistent Equations Including Exchange and Correlation Effects“. In: *Phys. Rev.* 140 (4A 1965), A1133–A1138. DOI: 10.1103/PhysRev.140.A1133. URL: https://link.aps.org/doi/10.1103/PhysRev.140.A1133.

[9] A. Georges and G. Kotliar. „Hubbard model in infinite dimensions“. In: *Phys. Rev. B* 45 (12 1992), pp. 6479–6483. DOI: 10.1103/PhysRevB.45.6479. URL: https://link.aps.org/doi/10.1103/PhysRevB.45.6479.

[10] W. Metzner and D. Vollhardt. „Correlated Lattice Fermions in d=∞ Dimensions“. In: *Phys. Rev. Lett.* 62 (3 1989), pp. 324–327. DOI: 10.1103/PhysRevLett.62.324. URL: https://link.aps.org/doi/10.1103/PhysRevLett.62.324.

[11] V. I. Anisimov, A. I. Poteryaev, M. A. Korotin, A. O. Anokhin, and G. Kotliar. „First-principles calculations of the electronic structure and spectra of strongly correlated systems: dynamical mean-field theory“. In: *Journal of Physics: Condensed Matter* 9.35 (1997), pp. 7359–7367. DOI: 10.1088/0953-8984/9/35/010. URL: https://doi.org/10.1088/0953-8984/9/35/010.

[12] A. I. Lichtenstein and M. I. Katsnelson. „Ab initio calculations of quasiparticle band structure in correlated systems: LDA++ approach“. In: *Physical Review B* 57.12 (1998), 6884–6895. ISSN: 1095-3795. DOI: 10.1103/physrevb.57.6884. URL: http://dx.doi.org/10.1103/PhysRevB.57.6884.

[13] J. Boust, A. Galler, S. Biermann, and L. V. Pourovskii. „Combining semilocal exchange with dynamical mean-field theory: Electronic structure and optical response of rare-earth sesquioxides“. In: *Phys. Rev. B* 105 (8 2022), p. 085133. DOI: 10.1103/PhysRevB.105.085133. URL: https://link.aps.org/doi/10.1103/PhysRevB.105.085133.

[14] A. Galler, J. Boust, A. Demourgues, S. Biermann, and L. V. Pourovskii. „Correlated electronic structure and optical response of rare-earth based semiconductors“. In: *Phys. Rev. B* 103 (24 2021), p. L241105. DOI: 10.1103/PhysRevB.103.L241105. URL: https://link.aps.org/doi/10.1103/PhysRevB.103.L241105.

[15] A. Waintal and J. Chenavas. In: *C. R. Acad. Sc. Ser. B* 264 (1967), pp. 168–170.

[16] R. D. Shannon. „Synthesis of some new perovskites containing indium and thallium“. In: *Inorganic Chemistry* 6.8 (1967), pp. 1474–1478. DOI: 10.1021/ic50054a009. eprint: https://doi.org/10.1021/ic50054a009. URL: https://doi.org/10.1021/ic50054a009.

[17] B. B. v. Aken, A. Meetsma, and T. T. M. Palstra. „Hexagonal $YMnO_3$“. In: *Acta Crystallographica Section C* 57.3 (2001), pp. 230–232. DOI: 10.1107/S0108270100015663. URL: https://doi.org/10.1107/S0108270100015663.

[18] C. Pistorius and G. Kruger. „Stability and structure of noncentrosymmetric hexagonal $LnInO_3$ (Ln = Eu, Gd, Tb, Dy, Ho, Y)“. In: *Journal of Inorganic and Nuclear Chemistry* 38.8 (1976), pp. 1471–1475. ISSN: 0022-1902. DOI: https://doi.org/10.1016/0022-1902(76)90011-7. URL: https://www.sciencedirect.com/science/article/pii/0022190276900117.

[19] H. L. Yakel Jnr, W. C. Koehler, E. F. Bertaut, and E. F. Forrat. „On the crystal structure of the manganese(III) trioxides of the heavy lanthanides and yttrium“. In: *Acta Crystallographica* 16.10 (1963), pp. 957–962. DOI: 10.1107/S0365110X63002589. URL: https://doi.org/10.1107/S0365110X63002589.

[20] F. Bertaut, F. Forrat, and P. Fang. In: *C. R. Acad. Sci.* 256 (1963), pp. 1958–1961.

[21] G. A. Smolenskiĭ and I. E. Chupis. „Ferroelectromagnets“. In: *Soviet Physics Uspekhi* 25.7 (1982), pp. 475–493. DOI: 10.1070/pu1982v025n07abeh004570. URL: https://doi.org/10.1070/pu1982v025n07abeh004570.

[22] B. B. Van Aken, J.-W. G. Bos, R. A. de Groot, and T. T. M. Palstra. „Asymmetry of electron and hole doping in $YMnO_3$“. In: *Phys. Rev. B* 63 (12 2001), p. 125127. DOI: 10.1103/PhysRevB.63.125127. URL: https://link.aps.org/doi/10.1103/PhysRevB.63.125127.

[23] B. B. Van Aken, T. T. Palstra, A. Filippetti, and N. A. Spaldin. „The origin of ferroelectricity in magnetoelectric $YMnO_3$“. In: *Nature Materials* 3.3 (2004), pp. 164–170. ISSN: 1476-4660. DOI: 10.1038/nmat1080. URL: https://doi.org/10.1038/nmat1080.

[24] K. Momma and F. Izumi. „VESTA 3 for three-dimensional visualization of crystal, volumetric and morphology data“. In: *Journal of Applied Crystallography* 44.6 (2011), pp. 1272–1276. DOI: 10.1107/S0021889811038970. URL: https://doi.org/10.1107/S0021889811038970.

[25] P. Villars and K. Cenzual, eds. *$YMnO_3$ Crystal Structure: Datasheet from "PAULING FILE Multinaries Edition – 2012" in SpringerMaterials*. Copyright 2016 Springer-Verlag Berlin Heidelberg & Material Phases Data System (MPDS), Switzerland & National Institute for Materials Science (NIMS), Japan. URL: https://materials.springer.com/isp/crystallographic/docs/sd_1219822.

[26] S. Samal, W. Green, S. Lofland, K. Ramanujachary, D. Das, and A. Ganguli. „Study on the solid solution of $YMn_{1-x}Fe_xO_3$: Structural, magnetic and dielectric properties". In: *Journal of Solid State Chemistry* 181.1 (2008), pp. 61–66. ISSN: 0022-4596. DOI: https://doi.org/10.1016/j.jssc.2007.10.032. URL: https://www.sciencedirect.com/science/article/pii/S0022459607004446.

[27] J. Krzystek, J. Telser, J. Li, and M. A. Subramanian. „Magnetic Properties and Electronic Structure of Manganese-Based Blue Pigments: A High-Frequency and -Field EPR Study". In: *Inorganic Chemistry* 54.18 (2015). PMID: 26340020, pp. 9040–9045. DOI: 10.1021/acs.inorgchem.5b01306. eprint: https://doi.org/10.1021/acs.inorgchem.5b01306. URL: https://doi.org/10.1021/acs.inorgchem.5b01306.

[28] A. Galler and L. V. Pourovskii. „Electronic structure of rare-earth mononitrides: quasiatomic excitations and semiconducting bands". In: *New Journal of Physics* 24.4 (2022), p. 043039. DOI: 10.1088/1367-2630/ac6317.

[29] M. Born and R. Oppenheimer. „Zur Quantentheorie der Molekeln". In: *Annalen der Physik* 389.20 (1927), pp. 457–484. DOI: https://doi.org/10.1002/andp.19273892002. eprint: https://onlinelibrary.wiley.com/doi/pdf/10.1002/andp.19273892002. URL: https://onlinelibrary.wiley.com/doi/abs/10.1002/andp.19273892002.

[30] D. C. Langreth and M. J. Mehl. „Beyond the local-density approximation in calculations of ground-state electronic properties". In: *Phys. Rev. B* 28 (4 1983), pp. 1809–1834. DOI: 10.1103/PhysRevB.28.1809. URL: https://link.aps.org/doi/10.1103/PhysRevB.28.1809.

[31] A. D. Becke. „Density-functional exchange-energy approximation with correct asymptotic behavior". In: *Phys. Rev. A* 38 (6 1988), pp. 3098–3100. DOI: 10.1103/PhysRevA.38.3098. URL: https://link.aps.org/doi/10.1103/PhysRevA.38.3098.

[32] J. P. Perdew et al. „Atoms, molecules, solids, and surfaces: Applications of the generalized gradient approximation for exchange and correlation". In: *Phys. Rev. B* 46 (11 1992), pp. 6671–6687. DOI: 10.1103/PhysRevB.46.6671. URL: https://link.aps.org/doi/10.1103/PhysRevB.46.6671.

[33] V. I. Anisimov, J. Zaanen, and O. K. Andersen. „Band theory and Mott insulators: Hubbard U instead of Stoner I“. In: *Phys. Rev. B* 44 (3 1991), pp. 943–954. DOI: 10.1103/PhysRevB.44.943. URL: https://link.aps.org/doi/10.1103/PhysRevB.44.943.

[34] V. I. Anisimov, I. V. Solovyev, M. A. Korotin, M. T. Czyżyk, and G. A. Sawatzky. „Density-functional theory and NiO photoemission spectra“. In: *Phys. Rev. B* 48 (23 1993), pp. 16929–16934. DOI: 10.1103/PhysRevB.48.16929. URL: https://link.aps.org/doi/10.1103/PhysRevB.48.16929.

[35] P. Blaha, K. Schwarz, F. Tran, R. Laskowski, G. K. H. Madsen, and L. D. Marks. „WIEN2k: An APW+lo program for calculating the properties of solids“. In: *The Journal of Chemical Physics* 152.7 (2020), p. 074101. DOI: 10.1063/1.5143061. eprint: https://doi.org/10.1063/1.5143061. URL: https://doi.org/10.1063/1.5143061.

[36] P. Blaha, K. Schwarz, G. K. H. Madsen, D. Kvasnicka, J. Luitz, R. Laskowski, F. Tran and L. D. Marks. *WIEN2k, An Augmented Plane Wave + Local Orbitals Program for Calculating Crystal Properties*. Karlheinz Schwarz, Techn. Universität Wien, Austria, 2018, ISBN 3-9501031-1-2.

[37] F. Tran and P. Blaha. „Accurate Band Gaps of Semiconductors and Insulators with a Semilocal Exchange-Correlation Potential“. In: *Phys. Rev. Lett.* 102 (22 2009), p. 226401. DOI: 10.1103/PhysRevLett.102.226401. URL: https://link.aps.org/doi/10.1103/PhysRevLett.102.226401.

[38] A. D. Becke and E. R. Johnson. „A simple effective potential for exchange“. In: *The Journal of chemical physics* 124.22 (2006), p. 221101. DOI: 10.1063/1.2213970.

[39] A. D. Becke and M. R. Roussel. „Exchange holes in inhomogeneous systems: A coordinate-space model“. In: *Phys. Rev. A* 39 (8 1989), pp. 3761–3767. DOI: 10.1103/PhysRevA.39.3761. URL: https://link.aps.org/doi/10.1103/PhysRevA.39.3761.

[40] P. Borlido, T. Aull, A. W. Huran, F. Tran, M. A. L. Marques, and S. Botti. „Large-Scale Benchmark of Exchange–Correlation Functionals for the Determination of Electronic Band Gaps of Solids“. In: *Journal of Chemical Theory and Computation* 15.9 (2019). PMID: 31306006, pp. 5069–5079. DOI: 10.1021/acs.jctc.9b00322. eprint: https://doi.org/10.1021/acs.jctc.9b00322. URL: https://doi.org/10.1021/acs.jctc.9b00322.

[41] F. Tran and P. Blaha. „Importance of the Kinetic Energy Density for Band Gap Calculations in Solids with Density Functional Theory“. In: *The Journal of Physical Chemistry A* 121.17 (2017). PMID: 28402113, pp. 3318–3325.

DOI: 10.1021/acs.jpca.7b02882. eprint: https://doi.org/10.1021/acs.jpca.7b02882. URL: https://doi.org/10.1021/acs.jpca.7b02882.

[42] J. C. Slater. „Wave Functions in a Periodic Potential“. In: *Phys. Rev.* 51 (10 1937), pp. 846–851. DOI: 10.1103/PhysRev.51.846. URL: https://link.aps.org/doi/10.1103/PhysRev.51.846.

[43] O. K. Andersen. „Linear methods in band theory“. In: *Phys. Rev. B* 12 (8 1975), pp. 3060–3083. DOI: 10.1103/PhysRevB.12.3060. URL: https://link.aps.org/doi/10.1103/PhysRevB.12.3060.

[44] D. D. Koelling and G. O. Arbman. „Use of energy derivative of the radial solution in an augmented plane wave method: application to copper“. In: *Journal of Physics F: Metal Physics* 5.11 (1975), pp. 2041–2054. DOI: 10.1088/0305-4608/5/11/016. URL: https://doi.org/10.1088/0305-4608/5/11/016.

[45] E Sjöstedt, L. Nordström, and D. Singh. „An Alternative Way of Linearizing the Augmented Plane-Wave Method“. In: *Solid State Communications* 114 (Mar. 2000), pp. 15–20. DOI: 10.1016/S0038-1098(99)00577-3.

[46] G. H. Wannier. „The Structure of Electronic Excitation Levels in Insulating Crystals“. In: *Phys. Rev.* 52 (3 1937), pp. 191–197. DOI: 10.1103/PhysRev.52.191. URL: https://link.aps.org/doi/10.1103/PhysRev.52.191.

[47] V. I. Anisimov et al. „Full orbital calculation scheme for materials with strongly correlated electrons“. In: *Phys. Rev. B* 71 (12 2005), p. 125119. DOI: 10.1103/PhysRevB.71.125119. URL: https://link.aps.org/doi/10.1103/PhysRevB.71.125119.

[48] O. Parcollet et al. „TRIQS: A toolbox for research on interacting quantum systems“. In: *Computer Physics Communications* 196 (2015), pp. 398 –415. ISSN: 0010-4655. DOI: http://dx.doi.org/10.1016/j.cpc.2015.04.023. URL: http://www.sciencedirect.com/science/article/pii/S0010465515001666.

[49] M. Aichhorn et al. „TRIQS/DFTTools: A TRIQS application for ab initio calculations of correlated materials“. In: *Computer Physics Communications* 204 (2016), pp. 200–208. ISSN: 0010-4655. DOI: https://doi.org/10.1016/j.cpc.2016.03.014. URL: https://www.sciencedirect.com/science/article/pii/S0010465516300728.

[50] M. Aichhorn et al. „Dynamical mean-field theory within an augmented plane-wave framework: Assessing electronic correlations in the iron pnictide LaFeAsO“. In: *Phys. Rev. B* 80 (8 2009), p. 085101. DOI: 10.1103/PhysRevB.80.085101. URL: https://link.aps.org/doi/10.1103/PhysRevB.80.085101.

[51] M. C. Gutzwiller. „Effect of Correlation on the Ferromagnetism of Transition Metals“. In: *Phys. Rev. Lett.* 10 (5 1963), pp. 159–162. DOI: 10.1103/PhysRevLett.10.159. URL: https://link.aps.org/doi/10.1103/PhysRevLett.10.159.

[52] J. Hubbard. „Electron Correlations in Narrow Energy Bands“. In: *Proceedings of the Royal Society of London. Series A, Mathematical and Physical Sciences* 276.1365 (1963), pp. 238–257. ISSN: 00804630. URL: http://www.jstor.org/stable/2414761.

[53] J. Kanamori. „Electron Correlation and Ferromagnetism of Transition Metals“. In: *Progress of Theoretical Physics* 30.3 (Sept. 1963), pp. 275–289. ISSN: 0033-068X. DOI: 10.1143/PTP.30.275. eprint: https://academic.oup.com/ptp/article-pdf/30/3/275/5278869/30-3-275.pdf. URL: https://doi.org/10.1143/PTP.30.275.

[54] A. M. Oleś. „Antiferromagnetism and correlation of electrons in transition metals“. In: *Phys. Rev. B* 28 (1 1983), pp. 327–339. DOI: 10.1103/PhysRevB.28.327. URL: https://link.aps.org/doi/10.1103/PhysRevB.28.327.

[55] A. A. Abrikosov, L. Gorkov, and I. E. Dzyaloshinski. *Methods of quantum field theory in statistical physics*. NJ, Prentice-Hall, 1963.

[56] K. Held. „Electronic structure calculations using dynamical mean field theory“. In: *Advances in physics* 56.6 (2007), pp. 829–926. URL: https://arxiv.org/abs/cond-mat/0511293.

[57] P. W. Anderson. „Localized Magnetic States in Metals“. In: *Phys. Rev.* 124 (1 1961), pp. 41–53. DOI: 10.1103/PhysRev.124.41. URL: https://link.aps.org/doi/10.1103/PhysRev.124.41.

[58] J. W. Negele and H. Orland. *Quantum Many-Particle Systems*. eng. Advanced book classics series. Reading, MA: Perseus Books, 1998. ISBN: 0738200522.

[59] M. Aichhorn, L. Pourovskii, and A. Georges. „Importance of electronic correlations for structural and magnetic properties of the iron pnictide superconductor LaFeAsO“. In: *Phys. Rev. B* 84 (5 2011), p. 054529. DOI: 10.1103/PhysRevB.84.054529. URL: https://link.aps.org/doi/10.1103/PhysRevB.84.054529.

[60] P. Seth, I. Krivenko, M. Ferrero, and O. Parcollet. „TRIQS/CTHYB: A continuous-time quantum Monte Carlo hybridisation expansion solver for quantum impurity problems“. In: *Computer Physics Communications* 200 (2016), pp. 274–284. ISSN: 0010-4655. DOI: https://doi.org/10.1016/j.cpc.2015.10.023. URL: https://www.sciencedirect.com/science/article/pii/S001046551500404X.

[61] W. Yang, A. J. Cohen, and P. Mori-Sánchez. „Derivative discontinuity, bandgap and lowest unoccupied molecular orbital in density functional theory“. In: *The Journal of Chemical Physics* 136.20 (2012), p. 204111. DOI: 10.1063/1.3702391. eprint: https://doi.org/10.1063/1.3702391. URL: https://doi.org/10.1063/1.3702391.

[62] H. Jiang. „Band gaps from the Tran-Blaha modified Becke-Johnson approach: A systematic investigation“. In: *The Journal of chemical physics* 138.13 (Apr. 2013), p. 134115. DOI: 10.1063/1.4798706.

[63] L. V. Pourovskii, B. Amadon, S. Biermann, and A. Georges. „Self-consistency over the charge density in dynamical mean-field theory: A linear muffin-tin implementation and some physical implications“. In: *Phys. Rev. B* 76 (23 2007), p. 235101. DOI: 10.1103/PhysRevB.76.235101. URL: https://link.aps.org/doi/10.1103/PhysRevB.76.235101.

[64] G. D. Mahan. *Many-particle physics*. 3rd ed. New York, NY: Kluwer Academic/Plenum Publishers, 2000, p. 160. ISBN: 0-306-46338-5.

[65] J. M. Tomczak. „Propriétés spectrales et optiques des Matériaux corrélés.“ Physique [physics]. Theses. Ecole Polytechnique X, Sept. 2007. Francais. pastel-00003163, pp. 41–73. URL: https://pastel.archives-ouvertes.fr/pastel-00003163.

[66] L. Ley. „Photoemission and optical properties“. In: *The Physics of Hydrogenated Amorphous Silicon II: Electronic and Vibrational Properties*. Ed. by J. D. Joannopoulos and G. Lucovsky. Berlin, Heidelberg: Springer Berlin Heidelberg, 1984, pp. 61–168. ISBN: 978-3-540-38847-0. DOI: 10.1007/3540128077_3. URL: https://doi.org/10.1007/3540128077_3.

[67] J. M. Tomczak, L. V. Pourovskii, L. Vaugier, A. Georges, and S. Biermann. „Rare-earth vs. heavy metal pigments and their colors from first principles“. In: *Proceedings of the National Academy of Sciences* 110.3 (2013), pp. 904–907. DOI: 10.1073/pnas.1215066110. eprint: https://www.pnas.org/doi/pdf/10.1073/pnas.1215066110. URL: https://www.pnas.org/doi/abs/10.1073/pnas.1215066110.

[68] P. Kubelka and F. Munk. „Ein Beitrag zur Optik der Farbanstriche“. In: *Z. Tech. Phys.* 12 (1931), pp. 593–601.

[69] P. Kubelka. „New Contributions to the Optics of Intensely Light-Scattering Materials. Part I“. In: *J. Opt. Soc. Am.* 38.5 (1948), pp. 448–457. DOI: 10.1364/JOSA.38.000448. URL: http://opg.optica.org/abstract.cfm?URI=josa-38-5-448.

[70] CIE. *Proceedings of the International Commission on Illumination, 1931*. Cambridge University Press, Cambridge, United Kingdom, 1932.

[71] T Smith and J Guild. „The C.I.E. colorimetric standards and their use“. In: *Transactions of the Optical Society* 33.3 (1931), pp. 73–134. DOI: 10.1088/1475-4878/33/3/301. URL: https://doi.org/10.1088/1475-4878/33/3/301.

[72] K. Nassau. *The Physics and Chemistry of Color : The Fifteen Causes of Color*. 2nd ed. Wiley Series in Pure and Applied Optics. New York, NY: Wiley, 2001. ISBN: 0471391069.

[73] *CIE Standard Illuminants for Colorimetry*. ISO 10526:1999/CIE S005:1998. 1999.

[74] R. Shukla, F. N. Sayed, V. Grover, S. K. Deshpande, A. Guleria, and A. K. Tyagi. „Quest for Lead Free Relaxors in $YIn_{1-x}Fe_xO_3$ ($0.0 \leq x \leq 1.0$) System: Role of Synthesis and Structure“. In: *Inorganic Chemistry* 53.19 (2014). PMID: 25207665, pp. 10101–10111. DOI: 10.1021/ic5009472. eprint: https://doi.org/10.1021/ic5009472. URL: https://doi.org/10.1021/ic5009472.

[75] T. Biswas and M. Jain. „Quasiparticle band structure and optical properties of hexagonal-$YMnO_3$“. In: *Journal of Applied Physics* 120.15 (2016), p. 155102. DOI: https://doi.org/10.1063/1.4964690.

[76] P. Werner, A. Comanac, L. de'Medici, M. Troyer, and A. J. Millis. „Continuous-Time Solver for Quantum Impurity Models“. In: *Phys. Rev. Lett.* 97 (7 2006), p. 076405. DOI: 10.1103/PhysRevLett.97.076405. URL: https://link.aps.org/doi/10.1103/PhysRevLett.97.076405.

[77] M. Anderson, R. Motta, S. Chandrasekar, and M. Stokes. „Proposal for a Standard Default Color Space for the Internet - sRGB“. In: *Proc. IS&T 4th Color and Imaging Conf.* Society for Imaging Science and Technology. 1996, pp. 238–245.

[78] P. Blaha, K. Schwarz, F. Tran, R. Laskowski, G. K. H. Madsen, and L. D. Marks. *WIEN2k An Augmented Plane Wave Plus Local Orbitals Program for Calculating Crystal Properties, User's Guide, WIEN2k_21.1 (Release 04/30/2021)*. http://susi.theochem.tuwien.ac.at/reg_user/textbooks/usersguide.pdf. Accessed: April 26 2022.

[79] A. Kokalj. „XCrySDen—a new program for displaying crystalline structures and electron densities“. In: *Journal of Molecular Graphics and Modelling* 17.3 (1999). Code available from http://www.xcrysden.org/, pp. 176–179. ISSN: 1093-3263. DOI: https://doi.org/10.1016/S1093-3263(99)00028-5. URL: https://www.sciencedirect.com/science/article/pii/S1093326399000285.